

Geometric Extended State Observer on SE(3) with Fast Finite-Time Stability: Theory and Validation on a Rotorcraft Aerial Vehicle

Ningshan Wang, Reza Hamrah, Amit K. Sanyal, Mark N. Glauser

^a*Department of Mechanical & Aerospace Engineering, Syracuse University, Syracuse, NY 13244, US*

Abstract

This article presents an extended state observer for vehicle modeled as a rigid body in three-dimensional translational and rotational motions. The extended state observer is applicable to a rotorcraft aerial vehicle with a fixed plane of rotors, modeled as an under-actuated system on the tangent bundle of the six-dimensional Lie group of rigid body motions, SE(3). The extended state observer is designed to estimate the resultant external disturbance force and disturbance torque acting on the vehicle. It guarantees stable convergence of disturbance estimation errors in finite time when the disturbances are constant and finite time convergence to a bounded neighborhood of zero errors for time-varying disturbances. This extended state observer design is based on a Hölder-continuous fast finite time stable differentiator that is similar to the super-twisting algorithm, to obtain fast convergence. Numerical simulations are conducted to validate the proposed extended state observer. The proposed extended state observer is compared with other existing research to show its advantages. A set of experimental results implementing disturbance rejection control using feedback of disturbance estimates from the extended state observer is also presented.

Keywords: Geometric Mechanics, Extended State Observer, Fast Finite-Time Stability, Unmanned Aerial Vehicle

1. Introduction

Rotorcraft unmanned aerial vehicles (UAVs) are increasingly being used in various applications, such as security and monitoring, infrastructure inspection, agriculture, wildland management, package delivery, and remote sensing. However, these UAVs are frequently exposed to dynamic uncertainties and disturbances caused by turbulence induced by airflow around structures or regions. Therefore, it is crucial to ensure robust flight control performance in such challenging environments, with guaranteed stability margins even in the presence of dynamic disturbances and uncertainties.

Recent research articles on rotorcraft UAV tracking control have used various methods to tackle the adverse effects of disturbances and uncertainties during the flight. Torrente et al. (2021) use Gaussian processes to complement the nominal dynamics of the multi-rotor in a model predictive control (MPC) pipeline. Hanover et al. (2021) use an explicit scheme to discretize the dynamics for a nonlinear MPC solved by optimization. Bangura and Mahony (2017) use the propeller aerodynamics as a direct feedforward term on the desired thrust to re-regulate the thrust command of the rotors. Craig et al. (2020) implement a set of pitot tubes onto the multi-rotor aircraft to directly sense the aircraft's airspeed. With the knowledge of propeller aerodynamic characteristics, the airspeed is then utilized to obtain the disturbance forces and torques as feedforward terms to

enhance control performance. Bisheban and Lee (2020) use artificial neural networks to obtain disturbance forces and torques with the kinematics information of the aircraft and then use the baseline control scheme based on the article by Lee et al. (2010) in their tracking control scheme design. The methods used in these research articles either need high computational efforts Torrente et al. (2021); Hanover et al. (2021); Bisheban and Lee (2020) or require precise modeling of the aerodynamic characteristics of the rotorcraft propellers Bangura and Mahony (2017); Craig et al. (2020), to obtain satisfactory control performance against disturbances.

In this article, we develop and use extended state observers to estimate disturbance force and disturbance torque vectors acting on a rotorcraft UAV. Extended state observers, along with disturbance observers and unknown input observers, are commonly used in association with the robust control technique known as *active disturbance rejection control* (ADRC), which can be traced back to the dissertation by Hartlieb (1956). In an ADRC scheme, estimates of unknown disturbance inputs from a disturbance observer (DO) or an extended state observer (ESO) are first obtained and then utilized in the control design to reject the disturbance. See, for example, Huang et al. (2001); Shao et al. (2018); Mechali et al. (2021); Cui et al. (2021) on application of ESO and Chen (2003); Liu et al. (2022); Bhale et al. (2022); Sanyal (2022) on application of DO in ADRC schemes. Jia et al. (2022) employ the disturbance model obtained by Faessler et al. (2017) and then estimate the drag coefficient as a parameter. This disturbance model is also employed by Moeini et al. (2021).

There are several methods to ensure the stability of ESO/DO designs used for rotorcraft tracking control. The linear ESO by Shao et al. (2018) is asymptotically stable (AS). Mechali et al. (2021) use the concept of geometric homogeneity Rosier (1992) to obtain an FTS ESO. A similar method is proposed in the ESO design by Guo and Zhao (2011). The Lyapunov functions/candidates used in the ESO stability analysis by Mechali et al. (2021) and Guo and Zhao (2011) are based on Rosier (1992), and are implicit. Jia et al. (2022), Moeini et al. (2021) and Liu et al. (2022) use variants of the DO proposed by Chen (2003). Another approach is to use the super-twisting algorithm (STA) Moreno and Osorio (2012) to design ESO. Xia et al. (2010) use this method in ESO design for spacecraft attitude control, and Cui et al. (2021) design an adaptive super-twisting ESO using a similar method for an ADRC scheme applied to rotorcraft UAV.

In much of the prior literature for rotorcraft UAV attitude control with ESO/DO for disturbance torque estimation and rejection in rotational dynamics, the attitude kinematics of the ESO/DO are either based on local linearization or represented using local coordinates (like Euler angles) or quaternions. Local coordinate representations can have singularity issues (e.g., gimbal lock with Euler angles), while quaternion representations may cause instability due to unwinding Bhat and Bernstein (2000b); Chaturvedi et al. (2011). In situations where the UAVs have to carry out aggressive maneuvers, as in rapid collision avoidance for example, disturbance estimation and rejection from such schemes may not be reliable or accurate enough for precise control of the UAV.

This article presents an ESO on $SE(3)$ for rotorcraft UAVs to provide reliable disturbance estimation under complex and challenging aerodynamic environments. The ESO on $SE(3)$ estimates the disturbance forces and torques during the flight of a UAV in both translational and rotational dimension. The proposed ESO is fast finite-time stable (FFTS), abbreviated as FFTS-ESO. This FFTS-ESO design is based on a novel Hölder-continuous fast finite-time stable differentiator (HC-FFTS-ESO). We carry out several sets of numerical simulations to show the validity of the proposed FFTS-ESO. Moreover, the proposed FFTS-ESO is compared with other existing research to show its advantages in the conducted simulations. A set of experimental results implementing a distur-

bance rejection mechanism using feedback of disturbance estimates from the FFTS-ESO is also presented. In the experiment, we hover the UAV in front of the turbulent flows generated by a fan array wind tunnel (FAWT). We obtain statistical information from the hot-wire measurements on the turbulent incoming flows. We observe the pose of the UAV to evaluate its flight control performance.

We highlight some unique contributions of this article.

- The proposed ESO is the major contribution of this article. The pose of the rotorcraft is represented directly on the Lie group of rigid body transformations, the special Euclidean group $SE(3)$. Unlike the ESO and DO designs reported by Mechali et al. (2021), Shao et al. (2018), and Cui et al. (2021), which use Euler angles or quaternions for attitude representation or do not include attitude kinematics, like the DO by Bhale et al. (2022) in disturbance torque estimation, the pose of the aircraft in this article is represented in $SE(3)$ to avoid kinematic singularities. We do not use local coordinates (like Euler angles) or (dual) quaternions for pose representation so that we avoid singularities due to local coordinate representations or quaternion unwinding, as reported by Bhat and Bernstein (2000b), and Chaturvedi et al. (2011). To the best of the author’s knowledge, there is no existing publication on aircraft disturbance observation using ESO with pose representation on $SE(3)$.
- The proposed FFTS-ESO is based on the HC-FFTSD. The commonly used geometric homogeneity method Rosier (1992); Guo and Zhao (2011); Liu et al. (2019); Wang and Sanyal (2021, 2022), cannot provide a straightforward (or explicit) Lyapunov function to prove the finite-time stability of the scheme. The (implicit) form of their Lyapunov functions is by Rosier (1992). This implicit Lyapunov function complicates the robustness analysis under measurement noise and time-varying disturbances when that analysis is essential for an ESO designed for disturbance estimation in ADRC schemes. We propose HC-FFTSD as an approach inspired by the STA Moreno and Osorio (2012); Vidal et al. (2016) of sliding-mode control (SMC). This approach gives a straightforward design of a strict Lyapunov function, which is explicit, and therefore avoids the weakness mentioned above.
- Based on the HC-FFTSD, the proposed FFTS-ESO schemes are both FFTS and Hölder-continuous, unlike the common STA and other FTS schemes that use discontinuous methods like terminal sliding-mode. Therefore, the proposed FFTS-ESO avoids the potentially harmful chattering phenomenon Sanyal and Bohn (2015), while maintaining FTS convergence.
- With explicit Lyapunov function in the stability analysis, we present proof of the robustness of the proposed FFTS-ESO under time-varying disturbing forces, torques, and measurement noise. To the best of the authors’ knowledge, there is no prior research on the noise robustness of ESO using Lyapunov analysis.

The remainder of the article is as follows. Section 2 presents some preliminary results that are needed to obtain sufficient conditions for the stability of the ESO and ADRC schemes. HC-FFTSD is presented, along with its stability and robustness analysis in Section 3. In Section 4, the ESO design problem is formulated. Section 5 describes the detailed FFTS-ESO design, which is based on the differentiator design in Section 3. Numerical simulations are conducted in Section 6. Section 7 describes the conducted UAV flight experiment with the UAV exposed to the disturbances generated by the FAWT in details. We conclude the paper, in Section 8, by summarizing the results and highlighting directions for forthcoming research.

2. Preliminaries

The statements and definitions in this section are used in the technical results obtained in later sections. The statements given here give the conditions under which a continuous time system is finite-time stable, fast finite-time stable, and practically finite-time stable using Lyapunov analysis, and the last statement is used in developing the main result.

Lemma 1 (Finite-time stable). Bhat and Bernstein (2000a) *Consider the following system of differential equations,*

$$\dot{x}(t) = f(x(t)), \quad f(0) = 0, \quad x(0) = x_0, \quad (1)$$

where $f : \mathcal{D} \rightarrow \mathbb{R}^n$ is continuous on an open neighborhood $\mathcal{D} \subset \mathbb{R}^n$ of the origin, and let there be a continuous and differentiable function $V(x(t))$ that is positive definite. Let the time derivative of $V(x)$ satisfy the following inequality:

$$\dot{V} \leq -\lambda V^\alpha, \quad (2)$$

where $x(t) \in \mathcal{D} \setminus \{0\}$, $\lambda > 0$, $\alpha \in]0, 1[$. Then the system (1) is FTS at the origin, which means $\forall x_0 \in \mathcal{D}$, x can reach the origin in finite time. Moreover, the settling time T , the time needed to reach the origin, satisfies

$$T \leq \frac{V^{1-\alpha}(x_0)}{\lambda(1-\alpha)}. \quad (3)$$

Lemma 2 (Fast finite-time stable). Yu et al. (2005) *Consider the system (1) and let there be a continuous and differentiable function $V(x(t))$ that is positive definite. Let the time derivative of $V(x)$ satisfy the following inequality:*

$$\dot{V} \leq -\lambda_1 V - \lambda_2 V^\alpha, \quad (4)$$

where $x(t) \in \mathcal{D} \setminus \{0\}$, $\lambda_1, \lambda_2 > 0$, $\alpha \in]0, 1[$. Then the system (1) is FFTS at the origin and the settling time T satisfies:

$$T \leq \frac{1}{\lambda_1(1-\alpha)} \ln \frac{\lambda_1 V^{1-\alpha}(x_0) + \lambda_2}{\lambda_2}. \quad (5)$$

Lemma 3 (Practically finite-time stable). Yu et al. (2005); Zhu et al. (2011) *Consider the system (1) and let there be a continuous and differentiable function $V(x)$ that is positive definite. Let the time derivative of $V(x)$ satisfy the following inequality:*

$$\dot{V} \leq -\lambda_1 V - \lambda_2 V^\alpha + \eta, \quad (6)$$

with $x(t) \in \mathcal{D} \setminus \{0\}$, $\lambda_1, \lambda_2 > 0$, and $\alpha \in]0, 1[$. Then the system (1) is practical finite-time stable (PFTS) at the origin, which means that the solution of (1) will converge to the following set in finite time

$$\left\{ x \mid V(x) \leq \min \left\{ \frac{\eta}{(1-\theta_0)\lambda_1}, \left(\frac{\eta}{(1-\theta_0)\lambda_2} \right)^{\frac{1}{\alpha}} \right\} \right\},$$

where $0 < \theta_0 < 1$. The settling time T is bounded above as follows:

$$T \leq \max \left\{ t_0 + \frac{1}{\theta_0 \lambda_1 (1-\alpha)} \ln \frac{\theta_0 \lambda_1 V^{1-\alpha}(x_0) + \lambda_2}{\lambda_2}, t_0 + \frac{1}{\lambda_1 (1-\alpha)} \ln \frac{\lambda_1 V^{1-\alpha}(x_0) + \theta_0 \lambda_2}{\theta_0 \lambda_2} \right\}.$$

Lemma 4. Hardy et al. (1952) *Let x and y be non-negative real numbers and let $p \in]1, 2[$. Then*

$$x^{\frac{1}{p}} + y^{\frac{1}{p}} \geq (x + y)^{\frac{1}{p}}. \quad (7)$$

Moreover, the above inequality is a strict inequality if both x and y are non-zero.

Definition 1. *Define $H : \mathbb{R}^3 \times \mathbb{R} \rightarrow \text{Sym}(3)$, the space of symmetric 3×3 matrices, as follows:*

$$H(x, k) := I - \frac{2k}{x^{\text{T}}x} xx^{\text{T}}. \quad (8)$$

Lemma 5. *Let $\mu \in \mathbb{R}^n \setminus \{0\}$ and $\alpha \in]0, 1/2[$. Consider $\mathcal{D} : \mathbb{R}^n \setminus \{0, -\mu\} \rightarrow \mathbb{R}^+$ as:*

$$\begin{aligned} \phi(x) &:= Y(x)^{\text{T}}Y(x), \text{ where} \\ Y(x) &:= \|x\|^{-2\alpha}x - \|x + \mu\|^{-2\alpha}(x + \mu). \end{aligned} \quad (9)$$

The global maximum of $\phi(x)$ is at $x = -\mu/2$.

We provide the proof of Lemma 5 in the appendix.

3. Hölder-Continuous Fast Finite-Time Stable Differentiator (HC-FFTSD)

In this section, we design the error dynamics for the proposed ESO in Section 5 in the form of an HC-FFTSD. We analyze the stability and robustness of the proposed HC-FFTSD in this section, to support the development of the ESO design in Section 5. Theorem 1 gives the proposed HC-FFTSD with its stability properties. Corollary 1 describes the convergence performance of the differentiator under external disturbances. Corollary 2 describes the convergence performance of the differentiator under measurement noise. In the analysis that follows, $e_1 \in \mathbb{R}^n$ stands for the measurement estimation error and $e_2 \in \mathbb{R}^n$ stands for the disturbance estimation error in the ESO error dynamics, respectively. In this section and the remainder of this paper, we denote the minimum and maximum eigenvalues of a matrix by $\lambda_{\min}(\cdot)$ and $\lambda_{\max}(\cdot)$, respectively.

Theorem 1. *Let $p \in]1, 2[$ and $k_3 > 0$. Define $\phi_1(\cdot) : \mathbb{R}^n \rightarrow \mathbb{R}^n$ and $\phi_2(\cdot) : \mathbb{R}^n \rightarrow \mathbb{R}^n$ as follows:*

$$\begin{aligned} \phi_1(e_1) &= k_3 e_1 + (e_1^{\text{T}} e_1)^{\frac{1-p}{3p-2}} e_1, \\ \phi_2(e_1) &= k_3^2 e_1 + \frac{2k_3(2p-1)}{3p-2} (e_1^{\text{T}} e_1)^{\frac{1-p}{3p-2}} e_1 + \frac{p}{3p-2} (e_1^{\text{T}} e_1)^{\frac{2(1-p)}{3p-2}} e_1. \end{aligned} \quad (10)$$

Define the differentiator gains $k_1, k_2 > 0$ and $\mathcal{A}^ \in \mathbb{R}^{2 \times 2}$, as:*

$$\mathcal{A}^* = \begin{bmatrix} -k_1 & 1 \\ -k_2 & 0 \end{bmatrix}, \quad (11)$$

which makes \mathcal{A}^ a Hurwitz matrix. Thereafter, the differentiator design:*

$$\begin{aligned} \dot{e}_1 &= -k_1 \phi_1(e_1) + e_2, \\ \dot{e}_2 &= -k_2 \phi_2(e_1), \end{aligned} \quad (12)$$

ensures that $(e_1^{\text{T}}, e_2^{\text{T}}) \in \mathbb{R}^{2n}$ converges to the origin in a fast finite-time stable manner.

Proof. The proof of Theorem 1 is based on Theorem 1 by Vidal et al. (2016), and Theorem 1 by Moreno and Osorio (2012). Two properties of ϕ_1 and ϕ_2 are provided as follows.

Property 1 (P1): The Jacobian of $\phi_1(e_1)$, denoted $\phi_1'(e_1)$, is given as follows:

$$\phi_1'(e_1) = \frac{d\phi_1(e_1)}{de_1} = k_3 I + (e_1^\top e_1)^{\frac{1-p}{3p-2}} \left[I - \frac{2(p-1)}{3p-2} \frac{e_1 e_1^\top}{e_1^\top e_1} \right], \quad (13)$$

so that the following identity holds:

$$\phi_2(e_1) = \phi_1'(e_1) \phi_1(e_1) \quad (14)$$

Property 2 (P2): ϕ_1' is a positive definite matrix, which means $\forall w \in \mathbb{R}^{2n}, e_1 \in \mathbb{R}^n$,

$$\lambda_{\min}\{\phi_1'(e_1)\} \|w\|^2 \leq w^\top \phi_1'(e_1) w \leq \lambda_{\max}\{\phi_1'(e_1)\} \|w\|^2. \quad (15)$$

The maximum and minimum eigenvalues of $\phi_1'(e_1)$ employed in (15) are as given below:

$$\lambda_{\max}\{\phi_1'(e_1)\} = k_3 + (e_1^\top e_1)^{\frac{1-p}{3p-2}}, \quad (16)$$

$$\lambda_{\min}\{\phi_1'(e_1)\} = k_3 + (e_1^\top e_1)^{\frac{1-p}{3p-2}} \frac{p}{3p-2}. \quad (17)$$

From Theorem 5.5 by Chen Chen (1984), we know that for a Hurwitz matrix \mathcal{A}^* as in (11), $\forall \mathcal{Q}^* \in \mathbb{R}^{2 \times 2}$ where $\mathcal{Q}^* \succ 0$, the Lyapunov equation:

$$(\mathcal{A}^*)^\top \mathcal{P}^* + \mathcal{P}^* \mathcal{A}^* = -\mathcal{Q}^*, \quad (18)$$

has a unique solution $\mathcal{P}^* \succ 0$. Express the positive definite matrices \mathcal{P}^* and \mathcal{Q}^* in components as:

$$\mathcal{P}^* = \begin{bmatrix} p_{11} & p_{12} \\ p_{12} & p_{22} \end{bmatrix}, \quad \mathcal{Q}^* = \begin{bmatrix} q_{11} & q_{12} \\ q_{12} & q_{22} \end{bmatrix}.$$

With \mathcal{P}^* defined as the solution to (18), \mathcal{A}^* , \mathcal{P}^* and \mathcal{Q}^* can be augmented to $\mathcal{A}, \mathcal{P}, \mathcal{Q} \in \mathbb{R}^{2n \times 2n}$, as follows:

$$\mathcal{A} = \begin{bmatrix} -k_1 I & I \\ -k_2 I & 0 \end{bmatrix}, \quad \mathcal{P} = \begin{bmatrix} p_{11} I & p_{12} I \\ p_{12} I & p_{22} I \end{bmatrix}, \quad \mathcal{Q} = \begin{bmatrix} q_{11} I & q_{12} I \\ q_{12} I & q_{22} I \end{bmatrix}.$$

The augmented matrices $\mathcal{A}, \mathcal{P}, \mathcal{Q}$ defined above also satisfy a Lyapunov equation as given below:

$$\mathcal{A}^\top \mathcal{P} + \mathcal{P} \mathcal{A} = -\mathcal{Q}. \quad (19)$$

Further, the eigenvalues of \mathcal{P} and \mathcal{P}^* , are related such that $\lambda_{\min}\{\mathcal{P}^*\} = \lambda_{\min}\{\mathcal{P}\}$, and $\lambda_{\max}\{\mathcal{P}^*\} = \lambda_{\max}\{\mathcal{P}\}$. Similar relations hold for \mathcal{Q} and \mathcal{Q}^* . Thus, with \mathcal{P} as the solution to (19), we consider the following Lyapunov candidate:

$$V(e_1, e_2) = \zeta^\top \mathcal{P} \zeta, \quad (20)$$

where $\zeta \in \mathbb{R}^{2n}$ is defined as $\zeta := [\phi_1^\top(e_1), e_2^\top]^\top$ and \mathcal{P} is the augmented \mathcal{P}^* , which is the unique solution of (18) for a given $\mathcal{Q}^* \succ 0$. The upper and lower bounds of the Lyapunov candidate V in (20) are as given below:

$$\lambda_{\min}\{\mathcal{P}\} \|\zeta\|^2 \leq V(e_1, e_2) \leq \lambda_{\max}\{\mathcal{P}\} \|\zeta\|^2. \quad (21)$$

From (21), we obtain the following two inequalities:

$$\lambda_{\min} \{\mathcal{P}\} (e_1^T e_1)^{\frac{p}{3p-2}} \leq \lambda_{\min} \{\mathcal{P}\} \|\zeta\|^2 \leq V(e_1, e_2), \quad (22)$$

$$k_3^2 \lambda_{\min} \{\mathcal{P}\} e_1^T e_1 \leq \lambda_{\min} \{\mathcal{P}\} \|\zeta\|^2 \leq V(e_1, e_2). \quad (23)$$

$V(e_1, e_2)$ is differentiable everywhere except the subspace $\mathcal{S} = \{(e_1, e_2) \in \mathbb{R}^{2n} | e_1 = 0\}$. From (12) and Property (P1), we obtain the time derivative of ζ as follows,

$$\begin{aligned} \dot{\zeta} &= \begin{bmatrix} \phi_1'(e_1) \dot{e}_1 \\ \dot{e}_2 \end{bmatrix} = \begin{bmatrix} \phi_1'(e_1)(-k_1 \phi_1(e_1) + e_2) \\ -k_2 \phi_1'(e_1) \phi_1(e_1) \end{bmatrix} \\ &= \mathcal{D}(e_1) \mathcal{A} \zeta, \end{aligned} \quad (24)$$

where,

$$\begin{aligned} \mathcal{D}(e_1) &= \text{diag}[\phi_1'(e_1), \phi_1'(e_1)] \in \mathbb{R}^{2n \times 2n}, \\ \lambda_{\min} \{\mathcal{D}(e_1)\} &= \lambda_{\min} \{\phi_1'(e_1)\}. \end{aligned} \quad (25)$$

With the expression of $\dot{\zeta}$ in (24), we obtain the time derivative of $V(e_1, e_2)$ as

$$\begin{aligned} \dot{V} &= \dot{\zeta}^T \mathcal{P} \zeta + \zeta^T \mathcal{P} \dot{\zeta} \\ &= \zeta^T ((\mathcal{D}(e_1) \mathcal{A})^T \mathcal{P} + \mathcal{P} \mathcal{D}(e_1) \mathcal{A}) \zeta \\ &= -\zeta^T \bar{\mathcal{Q}}(e_1) \zeta. \end{aligned} \quad (26)$$

where $\bar{\mathcal{Q}}(e_1)$ is as

$$\begin{aligned} \bar{\mathcal{Q}}(e_1) &= (\mathcal{D}(e_1) \mathcal{A})^T \mathcal{P} + \mathcal{P} \mathcal{D}(e_1) \mathcal{A} = \begin{bmatrix} \bar{\mathcal{Q}}_{11}(e_1) & \bar{\mathcal{Q}}_{12}(e_1) \\ \bar{\mathcal{Q}}_{12}(e_1) & \bar{\mathcal{Q}}_{22}(e_1) \end{bmatrix}, \\ \bar{\mathcal{Q}}_{11}(e_1) &= 2(k_1 p_{11} + k_2 p_{12}) \phi_1'(e_1), \\ \bar{\mathcal{Q}}_{12}(e_1) &= (k_1 p_{12} + k_2 p_{22} - p_{11}) \phi_1'(e_1), \\ \bar{\mathcal{Q}}_{22}(e_1) &= -2p_{12} \phi_1'(e_1). \end{aligned} \quad (27)$$

With (27) and (19), we obtain $\bar{\mathcal{Q}} = \mathcal{Q} \mathcal{D}(e_1)$. Afterwards, with \mathcal{Q} , $\mathcal{D}(e_1) \succ 0$, as defined in (19) and (25), following inequality on their eigenvalues holds: With $\mathcal{Q} \succ 0$ and $\mathcal{D}(e_1) \succ 0$, we obtain following inequality on their eigenvalues,

$$\lambda_{\min} \{\mathcal{Q} \mathcal{D}(e_1)\} \geq \lambda_{\min} \{\mathcal{Q}\} \lambda_{\min} \{\mathcal{D}(e_1)\} > 0. \quad (28)$$

With Property 2, substituting (28) into (26), we obtain

$$\begin{aligned} \dot{V} &= -\zeta^T (\mathcal{Q} \mathcal{D}(e_1)) \zeta \\ &\leq -\lambda_{\min} \{\mathcal{Q} \mathcal{D}(e_1)\} \zeta^T \zeta \\ &\leq -\lambda_{\min} \{\mathcal{D}(e_1)\} \lambda_{\min} \{\mathcal{Q}\} \zeta^T \zeta \end{aligned} \quad (29)$$

With $\lambda_{\min} \{\mathcal{D}(e_1)\} = \lambda_{\min} \{\phi_1'(e_1)\}$, substituting (17) and (22) into (29), we obtain,

$$\begin{aligned}\dot{V} &\leq -\left[k_3 + (e_1^\top e_1)^{\frac{1-p}{3p-2}} \frac{p}{3p-2}\right] \lambda_{\min} \{\mathcal{Q}\} \zeta^\top \zeta \\ &\leq -\frac{\lambda_{\min} \{\mathcal{Q}\}}{\lambda_{\max} \{\mathcal{P}\}} \left[k_3 + \left(\frac{V}{\lambda_{\min} \{\mathcal{P}\}}\right)^{\frac{1-p}{p}} \frac{p}{3p-2}\right] V \\ &\leq -\gamma_1 V - \gamma_2 V^{\frac{1}{p}},\end{aligned}\tag{30}$$

where γ_1 and γ_2 are positive constants, defined as,

$$\begin{aligned}\gamma_1 &= k_3 \frac{\lambda_{\min} \{\mathcal{Q}\}}{\lambda_{\max} \{\mathcal{P}\}} = k_3 \frac{\lambda_{\min} \{\mathcal{Q}^*\}}{\lambda_{\max} \{\mathcal{P}^*\}}; \\ \gamma_2 &= \frac{\lambda_{\min} \{\mathcal{Q}\} \lambda_{\min} \{\mathcal{P}\}^{\frac{p-1}{p}}}{\lambda_{\max} \{\mathcal{P}\}} \frac{p}{3p-2} = \frac{\lambda_{\min} \{\mathcal{Q}^*\} \lambda_{\min} \{\mathcal{P}^*\}^{\frac{p-1}{p}}}{\lambda_{\max} \{\mathcal{P}^*\}} \frac{p}{3p-2}.\end{aligned}\tag{31}$$

Therefore, based on the inequality (30), Lemma 1 and Lemma 2, we conclude that the origin of the error dynamics (12) is finite-time stable and fast finite-time stable. \square

Corollary 1 (Disturbance Robustness). *Consider the proposed HC-FFTSD (12) in Theorem 1 under perturbation, $\delta = (\delta_1^\top, \delta_2^\top)^\top$, $\delta_1, \delta_2 \in \mathbb{R}^n$, and δ is bounded as $\|\delta\| \leq \bar{\delta}$. Thereafter, the differentiator under perturbation is as*

$$\begin{aligned}\dot{e}_1 &= -k_1 \phi_1(e_1) + e_2 + \delta_1, \\ \dot{e}_2 &= -k_2 \phi_2(e_1) + \delta_2.\end{aligned}\tag{32}$$

When γ_1 in (31) fulfills $\gamma_1 \geq \lambda_{\max} \{\mathcal{P}\} / \lambda_{\min} \{\mathcal{P}\}$, (32) is practically finite-time stable (PFTS).

Proof. Consider the Lyapunov stability analysis in Theorem 1. With the Lyapunov-candidate defined by (20) and the expression of the differentiator under perturbation in (32), we express the time derivative of (20) as follows:

$$\dot{V} \leq -\gamma_1 V - \gamma_2 V^{\frac{1}{p}} + 2\lambda_{\max} \{\mathcal{P}\} \bar{\delta} \|\zeta\|.\tag{33}$$

By applying Cauchy-Schwarz inequality and (21), from (33), we obtain,

$$\begin{aligned}\dot{V} &\leq -\gamma_1 V - \gamma_2 V^{\frac{1}{p}} + \lambda_{\max} \{\mathcal{P}\} \|\zeta\|^2 + \lambda_{\max} \{\mathcal{P}\} \bar{\delta}^2 \\ &\leq -\left(\gamma_1 - \frac{\lambda_{\max} \{\mathcal{P}\}}{\lambda_{\min} \{\mathcal{P}\}}\right) V - \gamma_2 V^{\frac{1}{p}} + \lambda_{\max} \{\mathcal{P}\} \bar{\delta}^2.\end{aligned}\tag{34}$$

Therefore, according to Lemma 3, with inequality (34), we conclude that the system (32), which is the differentiator (12) under disturbance δ , is practical finite time stable at the origin. \square

Corollary 2 (Noise Robustness). *Consider the proposed HC-FFTSD (12) in Theorem 1 under measurement noise μ , so that $\phi_1(e_1)$ and $\phi_2(e_1)$ in (10) are replaced by $\phi_1(e_1 + \mu)$ and $\phi_2(e_1 + \mu)$ in the differentiator, as follows:*

$$\begin{aligned}\dot{e}_1 &= -k_1 \phi_1(e_1 + \mu) + e_2 \\ \dot{e}_2 &= -k_2 \phi_2(e_1 + \mu),\end{aligned}\tag{35}$$

where μ is bounded as $\|\mu\| \leq \bar{\mu}$. When γ_1 in (31) fulfills $\gamma_1 \geq \lambda_{\max} \{\mathcal{P}\} / \lambda_{\min} \{\mathcal{P}\}$, (35) is practically finite-time stable (PFTS).

Proof. From (35), we obtain the following expression

$$\begin{aligned}
\dot{e}_1 &= -k_1\phi_1(e_1) + e_2 + k_1\phi_1^*(e_1, \mu), \\
\dot{e}_2 &= -k_2\phi_2(e_1) + k_2\phi_2^*(e_1, \mu), \\
\phi_1^*(e_1, \mu) &= -\phi_1(e_1 + \mu) + \phi_1(e_1), \\
\phi_2^*(e_1, \mu) &= -\phi_2(e_1 + \mu) + \phi_2(e_1).
\end{aligned} \tag{36}$$

From (10), we obtain

$$\begin{aligned}
\phi_1^*(e_1, \mu) &= -\phi_1(e_1 + \mu) + \phi_1(e_1) \\
&= -k_3\mu - \|e_1 + \mu\|^{\frac{2(1-p)}{3p-2}}(e_1 + \mu) + \|e_1\|^{\frac{2(1-p)}{3p-2}}e_1 \\
\phi_2^*(e_1, \mu) &= -\phi_2(e_1 + \mu) + \phi_2(e_1) \\
&= -k_3^2\mu - \frac{2k_3(2p-1)}{3p-2}\|e_1 + \mu\|^{\frac{2(1-p)}{3p-2}}(e_1 + \mu) - \frac{p}{3p-2}\|e_1 + \mu\|^{\frac{4(1-p)}{3p-2}}(e_1 + \mu) \\
&\quad + \frac{2k_3(2p-1)}{3p-2}\|e_1\|^{\frac{2(1-p)}{3p-2}}e_1 + \frac{p}{3p-2}\|e_1\|^{\frac{4(1-p)}{3p-2}}e_1.
\end{aligned}$$

Therefore, according to Lemma 5, we obtain the upper bounds of $\|\phi_1^*(e_1, \mu)\|$ and $\|\phi_2^*(e_1, \mu)\|$ as:

$$\begin{aligned}
\|\phi_1^*(e_1, \mu)\| &\leq k_3\bar{\mu} + 2^{\frac{2(p-1)}{3p-2}}(\bar{\mu})^{1-\frac{2(p-1)}{3p-2}} \\
\|\phi_2^*(e_1, \mu)\| &\leq k_3^2\bar{\mu} + \frac{2k_3(2p-1)}{3p-2}2^{\frac{2(p-1)}{3p-2}}(\bar{\mu})^{1-\frac{2(p-1)}{3p-2}} + \frac{p}{3p-2}2^{\frac{4(p-1)}{3p-2}}(\bar{\mu})^{1-\frac{4(p-1)}{3p-2}}.
\end{aligned}$$

Applying Corollary 1 and with the above bounds on $\|\phi_1^*(e_1, \mu)\|$ and $\|\phi_2^*(e_1, \mu)\|$, we conclude that the error dynamics (35) is PFST at the origin. \square

4. Problem Formulation

4.1. Coordinate frame definition

The configuration of the vehicle, modeled as a rigid body, is given by its position and orientation, which are together referred to as its pose. To define the pose of the vehicle, we fix a coordinate frame \mathcal{B} to its body and another coordinate frame \mathcal{I} that is fixed in space as the inertial coordinate frame. Define e_i as the unit vector along the i th coordinate axis for $i = 1, 2, 3$. Let $b \in \mathbb{R}^3$ denote the position vector of the origin of frame \mathcal{B} with respect to frame \mathcal{I} . Let $\text{SO}(3)$ denote the orientation (attitude), defined as the rotation matrix from frame \mathcal{B} to frame \mathcal{I} . The pose of the vehicle can be represented in matrix form as follows:

$$g = \begin{bmatrix} R & b \\ 0 & 1 \end{bmatrix} \in \text{SE}(3) \tag{37}$$

where $\text{SE}(3)$, the special Euclidean group, is the six-dimensional Lie group of rigid body motions. A diagram of guidance and trajectory tracking on $\text{SE}(3)$ through a set of waypoints is presented in Figure 1 as follows.

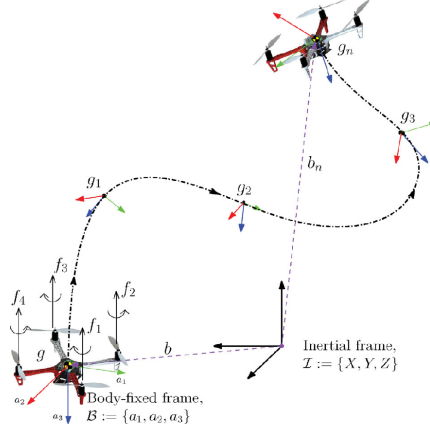


Figure 1: Guidance of a rotorcraft UAV through a trajectory between initial and final configurations on $SE(3)$ Hamrah and Sanyal (2022); Viswanathan et al. (2018)

4.2. System kinematics and dynamics

The instantaneous pose (position and attitude) is compactly represented by $g = (b, R) \in SE(3)$. The UAV's kinematics is then defined by:

$$\begin{cases} \dot{b} = v = R\nu, \\ \dot{R} = R\Omega^\times, \end{cases} \quad (38)$$

where $v \in \mathbb{R}^3$ and $\nu \in \mathbb{R}^3$ denote the translational velocity in frames \mathcal{I} and \mathcal{B} respectively, and $\Omega \in \mathbb{R}^3$ is the angular velocity in body-fixed frame \mathcal{B} . The overall system kinematics and dynamics of a rotorcraft UAV with a body-fixed plane of rotors are given by:

$$\begin{cases} \dot{b} = v = R\nu \\ m\dot{v} = mg\mathbf{e}_3 - fR\mathbf{e}_3 + \varphi_D \\ \dot{R} = R\Omega^\times \\ J\dot{\Omega} = J\Omega \times \Omega + \tau + \tau_D \end{cases} \quad (39)$$

where $\mathbf{e}_3 = [0 \ 0 \ 1]^\top$, $f \in \mathbb{R}$ is the scalar thrust force, and $\tau \in \mathbb{R}^3$ is the control torque created by the rotors, g denotes the acceleration due to gravity and $m \in \mathbb{R}^+$ and $J = J^\top \in \mathbb{R}^{3 \times 3}$ are the mass and inertia matrix of the UAV, respectively. The force and torque disturbances are denoted φ_D and τ_D respectively, which are mainly due to unsteady aerodynamics.

4.3. Morse function on $SO(3)$

The following Lemma is used for the rotational ESO scheme designed for the vehicle.

Lemma 6. Bohn and Sanyal (2016) *Consider attitude kinematics*

$$\dot{R} = R\Omega^\times, R \in SO(3), \Omega \in \mathfrak{so}(3). \quad (40)$$

Define $K = \text{diag}([K_1, K_2, K_3])$, where $K_1 > K_2 > K_3 \geq 1$. Define

$$s_K(R) = \sum_{i=1}^3 K_i (R^T \mathbf{e}_i) \times \mathbf{e}_i, \quad (41)$$

such that $\frac{d}{dt} \langle K, I - R \rangle = \Omega^T s_K(R)$. Here $\langle A, B \rangle = \text{tr}(A^T B)$, which makes $\langle K, I - R \rangle$ a Morse function defined on $\text{SO}(3)$. Let $\mathcal{S} \subset \text{SO}(3)$ be a closed subset containing the identity in its interior, defined by

$$\mathcal{S} = \{R \in \text{SO}(3) : R_{ii} \geq 0 \text{ and } R_{ij} R_{ji} \leq 0, \forall i, j \in \{1, 2, 3\}, i \neq j\}. \quad (42)$$

Then for $\forall R \in \mathcal{S}$, we have

$$s_K(R)^T s_K(R) \geq \langle K, I - R \rangle. \quad (43)$$

Remark 1 (Almost global domain of attraction). Sanyal et al. (2010) We know that the subset of $\text{SO}(3)$ where $s_K(R) = 0, R \in \text{SO}(3)$, which is also the set of critical points for $\langle I - R, K \rangle$, is

$$C \triangleq \{I, \text{diag}(1, -1, -1), \text{diag}(-1, 1, -1), \text{diag}(-1, -1, 1)\} \subset \text{SO}(3). \quad (44)$$

In addition, the global minimum of this Morse function is $R = I$.

4.4. ESO estimates and errors

The ESO design on $\text{SE}(3)$ is split into a translational ESO design on vector space \mathbb{R}^3 and a rotational ESO design on $\text{SO}(3)$. Let $(\hat{b}, \hat{v}, \hat{\varphi}_D) \in \mathbb{R}^3 \times \mathbb{R}^3 \times \mathbb{R}^3$ be the estimated position, translational velocity, and disturbance force, as the states of the translational ESO. The estimation errors for the translational ESO are defined as follows:

$$e_b = b - \hat{b}, e_v = v - \hat{v}, e_\varphi = \varphi_D - \hat{\varphi}_D, \quad (45)$$

which are estimation errors of position, translational velocity, and total disturbance force respectively.

Let $(\hat{R}, \hat{\Omega}, \hat{\tau}_D) \in \text{SO}(3) \times \mathbb{R}^3 \times \mathbb{R}^3$ be the estimated attitude, angular velocity, and disturbance torque states provided by the rotational ESO. For the rotational ESO, the error states are defined as follows. The attitude estimation error is defined as:

$$E_R = \hat{R}^T R, \quad (46)$$

on the group of rigid body rotations, $\text{SO}(3)$, which is not a vector space. The angular velocity estimation error, e_Ω , and torque disturbance estimation error, e_τ , are expressed on the vector space \mathbb{R}^3 , and are defined as:

$$e_\Omega = \Omega - E_R^T \hat{\Omega}, e_\tau = \tau_D - \hat{\tau}_D. \quad (47)$$

With a proper ESO design on $\text{SE}(3)$, the error states (e_b, e_v, e_φ) and (E_R, e_Ω, e_τ) should converge to $(0, 0, 0)$ and $(I, 0, 0)$, respectively. The ESO design and its stability proof are described in detail in the following section.

5. Fast Finite-Time Stable Extended State Observer (FFTS-ESO) on SE(3)

In this section, we present the FFTS-ESO on SE(3). As mentioned in the previous section, the ESO design on SE(3) can be represented as a translational ESO on the vector space \mathbb{R}^3 to estimate disturbance forces, and an rotational ESO on SO(3) to estimate disturbance torques. We present the two ESO designs along their stability proofs in this section.

5.1. ESO for Translational Motion

Proposition 1 (Translational ESO). *Define the positive scalar gains k_{t1} and k_{t2} , which make the matrix $\mathcal{A}_t \in \mathbb{R}^{2 \times 2}$ defined as:*

$$\mathcal{A}_t = \begin{bmatrix} -k_{t1} & 1 \\ -k_{t2} & 0 \end{bmatrix}, \quad (48)$$

a Hurwitz matrix. The ESO designed for the translational motion is given by:

$$\begin{aligned} \dot{\hat{b}} &= \hat{v}, \\ m\dot{\hat{v}} &= mg\mathbf{e}_3 - f\mathbf{R}\mathbf{e}_3 + mk_{t1}\phi_1(\psi_t) + m\kappa_t \left[(e_b^\top e_b)^{\frac{1-p}{p}} H\left(e_b, \frac{p-1}{p}\right) e_v + e_v \right] + \hat{\varphi}_D, \\ \dot{\hat{\varphi}}_D &= mk_{t2}\phi_2(\psi_t), \end{aligned} \quad (49)$$

where ψ_t is defined as

$$\psi_t = e_v + \kappa_t \left[e_b + (e_b^\top e_b)^{\frac{1-p}{p}} e_b \right], \quad \kappa_t > 1/2, \quad (50)$$

and $\phi_1(\cdot)$ is as defined by the expression in (10). In addition, the constant k_{t3} is defined and it occurs in the terms $\phi_1(\psi_t)$ and $\phi_2(\psi_t)$, where it takes the place of k_3 in (10).

Theorem 2. *With the observer errors for the translational ESO defined by (45), the translational kinematics and dynamics given by (39), and the ESO for translational motion given in Proposition 1, the error dynamics of the ESO is given by:*

$$\begin{aligned} \dot{e}_b &= e_v, \\ m\dot{e}_v &= -mk_{t1}\phi_1(\psi_t) - m\kappa_t \left[(e_b^\top e_b)^{\frac{1-p}{p}} H\left(e_b, \frac{p-1}{p}\right) e_v + e_v \right] + e_\varphi, \\ \dot{e}_\varphi &= -mk_{t2}\phi_2(\psi_t) + \dot{\varphi}_D. \end{aligned} \quad (51)$$

The error dynamics (51) is FFTS at the origin $((e_b, e_v, e_\varphi) = (0, 0, 0))$, when the resultant disturbance force is constant ($\dot{\varphi}_D = 0$) and the observer gains are constrained according to Proposition 1.

Proof. Simplify (51) as:

$$\begin{aligned} \dot{\psi}_t &= -k_{t1}\phi_1(\psi_t) + m^{-1}e_\varphi, \\ m^{-1}\dot{e}_\varphi &= -k_{t2}\phi_2(\psi_t) + m^{-1}\dot{\varphi}_D. \end{aligned} \quad (52)$$

Next, for \mathcal{A}_t as defined in (48), $\forall \mathcal{Q}_t \in \mathbb{R}^{2 \times 2}$ where $\mathcal{Q}_t \succ 0$, the Lyapunov equation,

$$\mathcal{A}_t^\top \mathcal{P}_t + \mathcal{P}_t \mathcal{A}_t = -\mathcal{Q}_t, \quad (53)$$

has a unique solution \mathcal{P}_t . Thereafter, define the Lyapunov function:

$$V_t = V_{t0} + \mu_t e_b^\top e_b, \text{ where } V_{t0} = \zeta_t^\top \mathcal{P}_t \zeta_t \quad (54)$$

and ζ_t is defined as:

$$\zeta_t = [\phi_1^\top(\psi_t), m^{-1} e_\varphi^\top]^\top.$$

We constrain the positive scalar μ_t in (54) as:

$$0 < \mu_t < k_{t3}^3 \frac{\lambda_{\min} \{\mathcal{P}_t\} \lambda_{\min} \{\mathcal{Q}_t\}}{\lambda_{\max} \{\mathcal{P}_t\}}. \quad (55)$$

From Theorem 1, (52) and (23), we find that the time-derivative of V_t satisfies:

$$\dot{V}_t \leq -\gamma_{t1} V_{t0} - \gamma_{t2} V_{t0}^{\frac{1}{p}} + 2\mu_t e_b^\top e_b, \quad (56)$$

where γ_{t1} and γ_{t2} are defined by:

$$\gamma_{t1} = k_{t3} \frac{\lambda_{\min} \{\mathcal{Q}_t\}}{\lambda_{\max} \{\mathcal{P}_t\}}, \quad \gamma_{t2} = \frac{\lambda_{\min} \{\mathcal{Q}_t\} \lambda_{\min} \{\mathcal{P}_t\}^{\frac{p-1}{p}} p}{\lambda_{\max} \{\mathcal{P}_t\} (3p-2)}. \quad (57)$$

Substituting (50) into (56), we obtain:

$$\begin{aligned} \dot{V}_t &\leq -\gamma_{t1} V_{t0} - \gamma_{t2} V_{t0}^{\frac{1}{p}} + 2\mu_t e_b^\top \left[\psi_t - \kappa_t e_b - \kappa_t (e_b^\top e_b)^{\frac{1-p}{p}} e_b \right] \\ &\leq -\gamma_{t1} V_{t0} - \gamma_{t2} V_{t0}^{\frac{1}{p}} + 2\mu_t e_b^\top \psi_t - 2\mu_t \kappa_t e_b^\top e_b - 2\mu_t \kappa_t (e_b^\top e_b)^{\frac{1}{p}} \\ &\leq -\gamma_{t1} V_{t0} - \gamma_{t2} V_{t0}^{\frac{1}{p}} - 2\mu_t \kappa_t e_b^\top e_b - 2\mu_t \kappa_t (e_b^\top e_b)^{\frac{1}{p}} + \mu_t \psi_t^\top \psi_t + \mu_t e_b^\top e_b \\ &\leq - \left(\gamma_{t1} - \frac{\mu_t}{k_{t3}^2 \lambda_{\min} \{\mathcal{P}_t\}} \right) V_{t0} - \gamma_{t2} V_{t0}^{\frac{1}{p}} - (2\kappa_t - 1) \mu_t e_b^\top e_b - 2\kappa_t \mu_t^{\frac{p-1}{p}} \mu_t^{\frac{1}{p}} (e_b^\top e_b)^{\frac{1}{p}}. \end{aligned} \quad (58)$$

Therefore, we further obtain:

$$\dot{V}_t < -\Gamma_{t1} V_t - \Gamma_{t2} V_t^{\frac{1}{p}}, \quad (59)$$

where

$$\begin{aligned} \Gamma_{t1} &= \min \left\{ k_{t3} \frac{\lambda_{\min} \{\mathcal{Q}_t\}}{\lambda_{\max} \{\mathcal{P}_t\}} - \frac{\mu_t}{k_{t3}^2 \lambda_{\min} \{\mathcal{P}_t\}}, 2\kappa_t - 1 \right\}, \\ \Gamma_{t2} &= \min \left\{ \frac{\lambda_{\min} \{\mathcal{Q}_t\} \lambda_{\min} \{\mathcal{P}_t\}^{\frac{p-1}{p}} p}{\lambda_{\max} \{\mathcal{P}_t\} (3p-2)}, 2\kappa_t \mu_t^{\frac{p-1}{p}} \right\}. \end{aligned} \quad (60)$$

Based on (59), we conclude that when the resultant disturbance force is constant and the ESO gains satisfy the constraints 1-3 in Proposition 1, the error dynamics of the ESO (51) is FFTS. This concludes the proof of Theorem 2. \square

5.2. ESO for Rotational Motion

Proposition 2 (Rotational ESO). Define $e_R = s_K(E_R)$, where $s_K(\cdot)$ is as defined by Lemma 6. Define $e_w(E_R, e_\Omega)$ as follows:

$$e_w(E_R, e_\Omega) = \frac{d}{dt}e_R = \sum_{i=1}^3 K_i \mathbf{e}_i \times (e_\Omega \times E_R^T \mathbf{e}_i). \quad (61)$$

Define the positive scalar gains k_{a1} and k_{a2} , which make the matrix $\mathcal{A}_a \in \mathbb{R}^{2 \times 2}$ defined as:

$$\mathcal{A}_a = \begin{bmatrix} -k_{a1} & 1 \\ -k_{a2} & 0 \end{bmatrix}, \quad (62)$$

a Hurwitz matrix. The ESO designed for the rotational motion is given by:

$$\begin{aligned} \dot{\hat{R}} &= \hat{R} \hat{\Omega}^\times, \\ \dot{\hat{\Omega}} &= E_R J^{-1} \left[J \Omega \times \Omega + \hat{\tau}_D + \tau + k_{a1} J \phi_1(\psi_a) + \kappa_a J (e_R^T e_R)^{\frac{1-p}{p}} H \left(e_R, \frac{p-1}{p} \right) e_w \right] \\ &\quad + E_R J^{-1} (\kappa_a J e_w) + E_R e_\Omega^\times E_R^T \hat{\Omega}, \\ \dot{\hat{\tau}}_D &= J k_{a2} \phi_2(\psi_a), \end{aligned} \quad (63)$$

where ψ_a is defined as follows:

$$\psi_a = e_\Omega + \kappa_a \left[e_R + (e_R^T e_R)^{\frac{1-p}{p}} e_R \right], \quad \kappa_a > \frac{1}{2}. \quad (64)$$

In addition, the constant k_{a3} is defined and it occurs in the terms $\phi_1(\psi_a)$ and $\phi_2(\psi_a)$, where it takes the place of k_3 in (10).

Theorem 3. With the observer errors for the rotational ESO defined by (47), the rotational kinematics and dynamics given by (39), and the ESO for rotational motion given in Proposition 2, the error dynamics of the ESO is given by:

$$\begin{aligned} \dot{E}_R &= E_R e_\Omega^\times, \\ J \dot{e}_\Omega &= -k_{a1} J \phi_1(\psi_a) - \kappa_a J \left[(e_R^T e_R)^{\frac{1-p}{p}} H \left(e_R, \frac{p-1}{p} \right) e_w + e_w \right] + e_\tau, \\ \dot{e}_\tau &= -k_{a2} J \phi_2(\psi_a) + \dot{\tau}_D. \end{aligned} \quad (65)$$

The error dynamics (65) is almost globally FFTS at the origin $((E_R, e_\Omega, e_\tau) = (I, 0, 0))$, when the resultant disturbance torque is constant ($\dot{\tau}_D = 0$) and the observer gains are constrained according to Proposition 2.

Proof. Simplify (65) as:

$$\begin{aligned} \dot{\psi}_a &= -k_{a1} \phi_1(\psi_a) + J^{-1} e_\tau, \\ J^{-1} \dot{e}_\tau &= -k_{a2} \phi_2(\psi_a) + J^{-1} \dot{\tau}_D. \end{aligned} \quad (66)$$

Next, for \mathcal{A}_a as defined in (62), $\forall \mathcal{Q}_a \in \mathbb{R}^{2 \times 2}$ where $\mathcal{Q}_a \succ 0$, the Lyapunov equation:

$$\mathcal{A}_a^T \mathcal{P}_a + \mathcal{P}_a \mathcal{A}_a = -\mathcal{Q}_a, \quad (67)$$

has a unique solution \mathcal{P}_a . Thereafter, define the Morse-Lyapunov function:

$$V_a = V_{a0} + \mu_a \langle K, I - E_R \rangle, \text{ where } V_{a0} = \zeta_a^T \mathcal{P}_a \zeta_a, \quad (68)$$

μ_a is a positive scalar, and ζ_a is defined as:

$$\zeta_a = [\phi_1^T(\psi_a), J^{-1} e_\tau^T]^T.$$

We constrain the positive scalar μ_a in (68) as:

$$0 < \mu_a < 2k_{a3}^3 \frac{\lambda_{\min} \{\mathcal{P}_a\} \lambda_{\min} \{\mathcal{Q}_a\}}{\lambda_{\max} \{\mathcal{P}_a\}}. \quad (69)$$

From Theorem 1, (66) and (23), we find that the time-derivative of V_a satisfies:

$$\dot{V}_a \leq -\gamma_{a1} V_{a0} - \gamma_{a2} V_{a0}^{\frac{1}{p}} + \mu_a e_R^T e_\Omega, \quad (70)$$

where γ_{a1} and γ_{a2} are defined by:

$$\gamma_{a1} = k_{a3} \frac{\lambda_{\min} \{\mathcal{Q}_a\}}{\lambda_{\max} \{\mathcal{P}_a\}}, \quad \gamma_{a2} = \frac{\lambda_{\min} \{\mathcal{Q}_a\} \lambda_{\min} \{\mathcal{P}_a\}^{\frac{p-1}{p}} p}{\lambda_{\max} \{\mathcal{P}_a\} (3p-2)}. \quad (71)$$

Substituting (64) into (70), we obtain:

$$\begin{aligned} \dot{V}_a &\leq -\gamma_{a1} V_{a0} - \gamma_{a2} V_{a0}^{\frac{1}{p}} + \mu_a e_R^T \left[\psi_a - \kappa_a e_R - \kappa_a (e_R^T e_R)^{\frac{1-p}{p}} e_R \right] \\ &\leq -\gamma_{a1} V_{a0} - \gamma_{a2} V_{a0}^{\frac{1}{p}} + \frac{1}{2} \mu_a \left(e_R^T e_R + \psi_a^T \psi_a \right) - \kappa_a \mu_a \left[e_R^T e_R + (e_R^T e_R)^{\frac{1}{p}} \right] \\ &\leq - \left(\gamma_{a1} - \frac{\mu_a}{2k_{a3}^2 \lambda_{\min} \{\mathcal{P}_a\}} \right) V_{a0} - \gamma_{a2} V_{a0}^{\frac{1}{p}} - \left(\kappa_a - \frac{1}{2} \right) \mu_a e_R^T e_R - \kappa_a \mu_a (e_R^T e_R)^{\frac{1}{p}}. \end{aligned} \quad (72)$$

By applying Lemma 6 on (70), we obtain:

$$\begin{aligned} \dot{V}_a &\leq - \left(\gamma_{a1} - \frac{\mu_a}{2k_{a3}^2 \lambda_{\min} \{\mathcal{P}_a\}} \right) V_{a0} - \gamma_{a2} V_{a0}^{\frac{1}{p}} \\ &\quad - \left(\kappa_a - \frac{1}{2} \right) \mu_a \langle K, I - E_R \rangle - \kappa_a \mu_a^{\frac{p-1}{p}} \mu_a^{\frac{1}{p}} \langle K, I - E_R \rangle^{\frac{1}{p}}. \end{aligned} \quad (73)$$

After some algebra, we further obtain:

$$\dot{V}_a \leq -\Gamma_{a1} V_a - \Gamma_{a2} V_a^{\frac{1}{p}}, \quad (74)$$

where:

$$\begin{aligned} \Gamma_{a1} &= \min \left\{ k_{a3} \frac{\lambda_{\min} \{\mathcal{Q}_a\}}{\lambda_{\max} \{\mathcal{P}_a\}} - \frac{\mu_a}{2k_{a3}^2 \lambda_{\min} \{\mathcal{P}_a\}}, \kappa_a - \frac{1}{2} \right\}, \\ \Gamma_{a2} &= \min \left\{ \frac{\lambda_{\min} \{\mathcal{Q}_a\} \lambda_{\min} \{\mathcal{P}_a\}^{\frac{p-1}{p}} p}{\lambda_{\max} \{\mathcal{P}_a\} (3p-2)}, \kappa_a \mu_a^{\frac{p-1}{p}} \right\}. \end{aligned} \quad (75)$$

Considering the expression given by (74), the set where $\dot{V}_a = 0$ is:

$$\begin{aligned} \dot{V}_a^{-1}(0) &= \{(E_R, e_\Omega, e_\tau) : s_K(E_R) = 0, \text{ and } \zeta_a = 0\} \\ &= \{(E_R, e_\Omega, e_\tau) : E_R \in C, e_\Omega = 0, \text{ and } e_\tau = 0\}, \end{aligned} \quad (76)$$

where C is as defined by (44), which gives the set of the critical points of the Morse function used as part of the Morse-Lyapunov function in (68). Using Theorem 8.4 from Khalil (2002), we conclude that (E_R, e_Ω, e_τ) converge to the set:

$$S = \{(E_R, e_\Omega, e_\tau) \in \text{SO}(3) \times \mathbb{R}^3 \times \mathbb{R}^3 : E_R \in C, e_\Omega = 0, \text{ and } e_\tau = 0\}, \quad (77)$$

in finite time. Based on (74), and Lemma 2, we conclude that when the observer gains satisfy the constraints in Proposition 2, the error dynamics (65) converges to the set S in finite time.

In S , the only stable equilibrium is $(I, 0, 0)$, while the other three are unstable. The resulting closed-loop system with the estimation errors gives rise to a Hölder-continuous feedback with exponent less than one ($1/2 < 1/p < 1$), while in the limiting case of $p = 1$, the feedback system is Lipschitz-continuous. Proceeding with a topological equivalence-based analysis similar to the one by Bohn and Sanyal (2016), we conclude that the equilibrium and the corresponding regions of attraction of the rotational ESO with $p \in]1, 2[$ are identical to those of the corresponding Lipschitz-continuous asymptotically stable ESO with $p = 1$, and the region of attraction is almost global.

To summarize, we conclude that the error dynamics (51) is almost globally FFTS (AG-FFTS) at the origin $((E_R, e_\Omega, e_\tau) = (I, 0, 0))$ when the resultant disturbance torque is constant ($\dot{\tau}_D = 0$) and the observer gains are constrained according to Proposition 2. This concludes the proof of Theorem 3. \square

Remark 2 (Disturbance robustness of the ESO). Consider Corollary 1 and its constraints on differentiator gains. When the disturbance forces and torques are time-varying, then $\|\dot{\varphi}_D\|, \|\dot{\tau}_D\| > 0$. Further, if the constraints on gains in Corollary 1 are fulfilled, the estimation error dynamics of the proposed ESO will be PFTS.

Remark 3 (Noise robustness of the ESO). Consider Corollary 2 and its constraints on differentiator gains. When the ESO measurements have noise and the constraints on gains in Corollary 2 are fulfilled, the estimation error dynamics of the proposed ESO will be PFTS. Moreover, according to Lemma 3 and Corollary 2, the η in (6) of Lemma 3 is a function on the level of noise in information on R, Ω, b and v and is monotonically increasing with the level of noise.

Remark 4 (Comparative Analysis of Noise Robustness: FFTS-ESO vs. the FxTSDO by Liu et al. Liu et al. (2022)). We investigate the disturbance (forces or torques) observers proposed by Liu et al. (2022) in their Theorems 1 and 2, known as FxTSDO. The input of FxTSDO relies on the motion signals, X_2, Y_2 , which represent translational and angular velocities, and \dot{X}_2, \dot{Y}_2 , which represent translational and angular accelerations, respectively. However, the high-level noise associated with the translational acceleration obtained from an accelerometer restricts its direct use in a flight control scheme. Additionally, direct measurement of angular acceleration is usually not feasible. Furthermore, if \dot{X}_2 and \dot{Y}_2 are obtained from the finite difference of X_2 and Y_2 , they will have higher noise levels than X_2 and Y_2 , leading to inferior disturbance estimation performance. In contrast to FxTSDO, the proposed FFTS-ESO incorporates position and attitude signals, which are zero-order derivatives of motions with lower noise levels. Consequently, FFTS-ESO outperforms FxTSDO in terms of disturbance estimation performance, despite the theoretical fixed-time stability of FxTSDO. We show this through our numerical simulations in Section 6.

6. Numerical Simulations

In this section, we compare the proposed FFTS-ESO with existing disturbance estimation schemes, which are LESO by Shao et al. (2018) and FxTSDO by Liu et al. (2022), on their disturbance estimation performance in four different simulated flight scenarios, with and without the presence of measurement noises. The four flight scenarios correspond to four desired trajectories. The inertia and mass of the simulated rotorcraft UAV are $J = \text{diag}([0.0820, 0.0845, 0.1377])$ kg · m², $m = 4.34$ kg by Pounds et al. (2010). Since the goal of the simulation is to validate and compare the disturbance estimation performance, the actuator dynamics and saturation are not included in the results reported in this section. The tracking control scheme to drive the UAV to track the desired trajectories is developed based on the control scheme reported by Viswanathan et al. (2017, 2018). As this scheme is not a contribution of this article, we omit its description for brevity. We use MATLAB/Simulink with its ODE2 (Heun method) solver to conduct this set of simulations. The time step size is $h = 0.001$ s and the simulated duration is $T = 30$ s.

Hovering	$b_d(t) = [0, 0, -3]^T$ (m)
Slow Swing	$b_d(t) = [10 \sin(0.1\pi t), 0, -3]^T$ (m)
Fast Swing	$b_d(t) = [5 \sin(0.5\pi t), 0, -3]^T$ (m)
High Pitch	$b_d(t) = [10 \sin(0.5\pi t), 10 \cos(0.5\pi t), -3]^T$ (m)

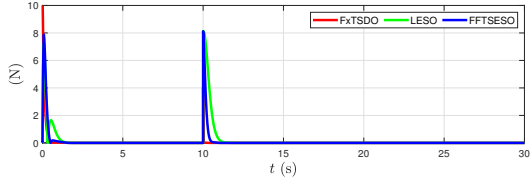
Table 1: Flight trajectories to be tracked for the comparisons between LESO, FxTSDO and FFTS-ESO

b_N	$b_N = b + \mu_b$	$\mu_b \sim P_b = 3e^{-8}$
v_N	$v_N = v + \mu_v$	$\mu_v \sim P_v = 3e^{-7}$
R_N	$R_N = R \exp(\mu_R)$	$\mu_R \sim P_R = 3e^{-8}$
Ω_N	$\Omega_N = \Omega + \mu_\Omega$	$\mu_\Omega \sim P_\Omega = 3e^{-7}$

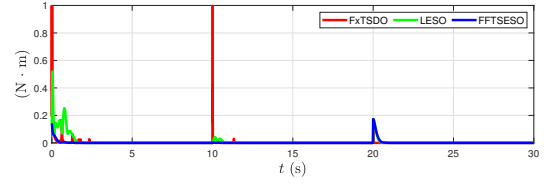
Table 2: Measurement noise level in power spectral density for the comparisons between LESO, FxTSDO, and FFTS-ESO

The four flight scenarios are the four desired trajectories listed in Table 1. ‘Hovering’ is the simplest flight scenario where the aircraft is ordered to hover at a fixed position during the simulation. ‘High Pitch’ is the most complex flight scenario where the aircraft has to pitch up and track a circular trajectory. Since the norm of centripetal acceleration in the ‘High Pitch’ scenario is more than a g , the aircraft has to flip over to track the desired trajectory. This desired trajectory with high centripetal acceleration forces the aircraft to go past the 90° pitch singularity of an Euler angle attitude representation. The measurement noise levels are as listed in Table 2 in terms of power spectral density (PSD). The disturbance force and torque in all of the four scenarios in this set of simulations are identical and they are the following step functions:

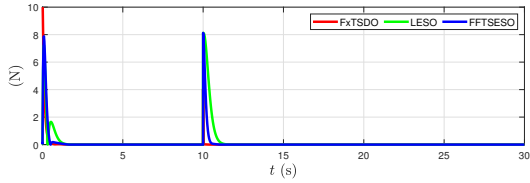
$$\varphi_D(t) = \begin{cases} [5, 10, 0]^T \text{ N} & t < 10 \text{ s} \\ [9, 15, 5]^T \text{ N} & t \geq 10 \text{ s} \end{cases}, \tau_D(t) = \begin{cases} [-0.1, 0.1, 0.1]^T \text{ N} \cdot \text{m} & t < 20 \text{ s} \\ [0, 0, 0.2]^T \text{ N} \cdot \text{m} & t \geq 20 \text{ s} \end{cases}$$



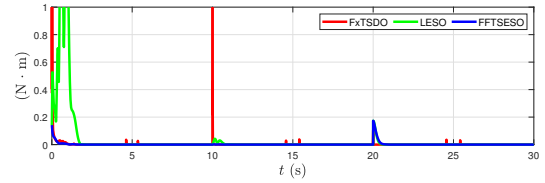
(a) Hover



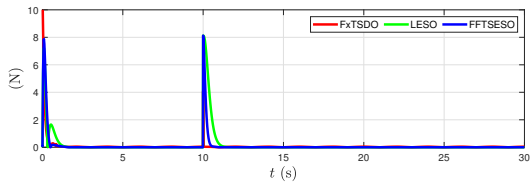
(a) Hover



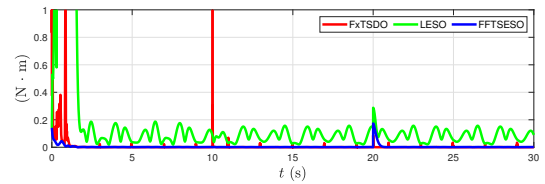
(b) Slow swing



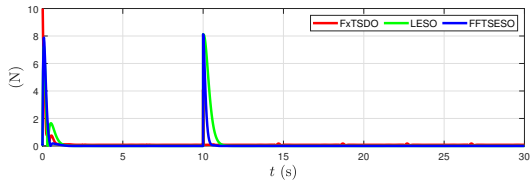
(b) Slow swing



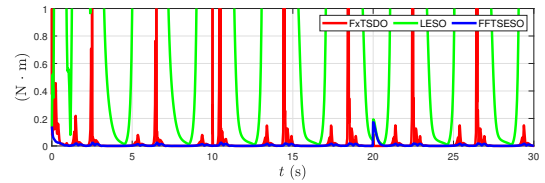
(c) Fast swing



(c) Fast swing



(d) High pitch



(d) High pitch

Figure 2: Disturbance force estimation errors of the UAV from FxTSDO, LESO, and FFTS-ESO, in four different tracking control scenarios without measurement noise.

Figure 3: Disturbance torque estimation errors of the UAV from FxTSDO, LESO, and FFTS-ESO, in four different tracking control scenarios without measurement noise.

The parameters for FFTS-ESO in these simulations are $p = 1.2, k_{t1} = 3, k_{t2} = 2, k_{t3} = 6, \kappa_t = 0.8, k_{a1} = 3, k_{a2} = 2, k_{a3} = 4, \kappa_a = 0.6$. The gains for FxTSDO and LESO are as given by Liu et al. (2022) and by Shao et al. (2018). In the simulated flight, the initial states of the UAV for all four scenarios are: $R(0) = I, \Omega(0) = [0, 0, 0]^T \text{ rad/s}, b(0) = [0.01, 0, 0]^T \text{ m}, v(0) = [5\pi, 0, 0]^T \text{ m/s}$. The initial conditions of the FxTSDO, LESO, and FFTS-ESO, are identical to the pose, velocities and disturbance of the UAV at the initial time in the simulation.

We present the simulation results in four sets of figures. Figure 2 and 3 present the disturbance force and torque estimation errors respectively, from FxTSDO, LESO and FFTS-ESO in the flight scenarios described in Table 1 with noise-free measurements. Figure 4 and 5 present the disturbance estimation errors from these schemes for the flight trajectories in Table 1, in the presence of measurement noise levels as described in Table 2.

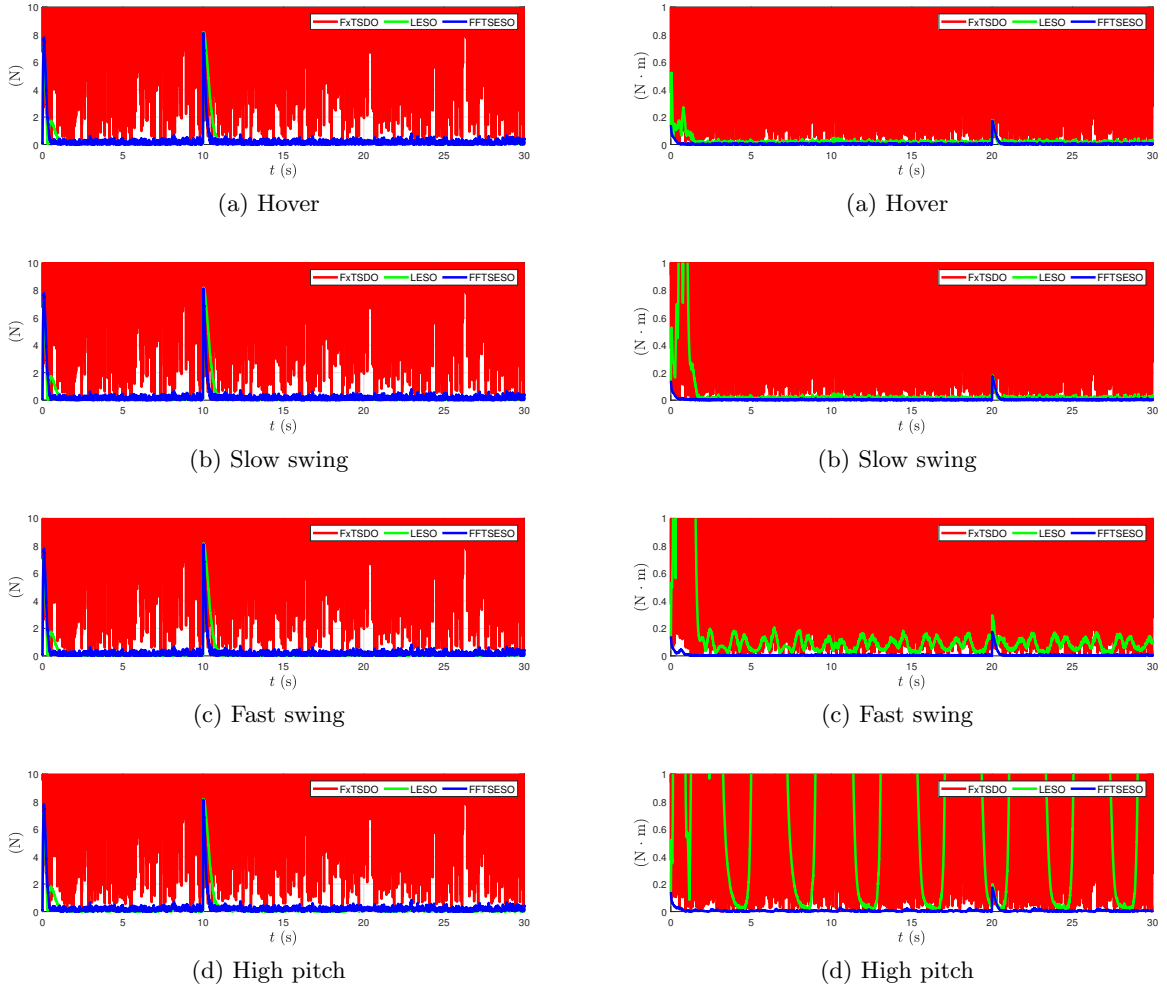


Figure 4: Disturbance force estimation errors of the UAV from FxTSDO, LESO, and FFTS-ESO, in four different tracking control scenarios with measurement noise. Figure 5: Disturbance torque estimation errors of the UAV from FxTSDO, LESO, and FFTS-ESO, in four different tracking control scenarios with measurement noise.

Figure 2 shows the disturbance force estimation errors from the three schemes with noise-free measurements. Although the disturbance force estimation error from FxTSDO shows significant

initial transient, the results from Figure 2 indicates that with noise-free measurement, the disturbance force estimations from these three schemes converge to the origin in all four flight scenarios. The transients at $t = 15$ s are from the step-function disturbance force φ_D , whose step time is $t = 15$ s. Figure 3 shows the disturbance torque estimation errors from the three schemes with noise-free measurement. In Figure 3, we observe that when $t = 10$ s, high transients appears in the disturbance torque estimation error from FxTSDO.

Despite the initial transients, the disturbance torque estimation errors from all three schemes converge to the origin in 'Hovering' and 'Slow swing' scenarios. However, in 'Fast swing' and 'High pitch' scenarios, the disturbance torque estimation errors from LESO and FxTSDO diverge. As is stated in Section 1, since the LESO uses Euler-angle to represent attitude for disturbance torque estimation, it experiences a singularity in attitude representation when the UAV tracks the 'Fast swing' and 'High Pitch' trajectories. Thus, in these two scenarios, the singularity in the attitude representation destabilizes the disturbance torque estimation error of LESO.

Figure. 4 and 5 present the disturbance force and disturbance torque estimation errors respectively, from the three schemes with identical noisy measurements as given in Table 2. As is stated in Remark 4, we observe that with measurement noise, FxTSDO is not capable of providing any meaningful disturbance estimation. In 'Fast swing' and 'High pitch' scenarios, the disturbance torque estimation errors from LESO diverge from the origin.

To summarize, figures 2, 3, 4, and 5 show that the FFTS-ESO has satisfactory disturbance estimation performance and outperforms the LESO and FxTSDO when the UAV experiences large pose changes and has noisy measurements.

7. Flight Experiments

In this section, the proposed FFTS-ESO is validated through flight experiments. Its hardware and software are custom-designed and developed based on the open-source autopilot PX4 by Meier et al. (2015). To demonstrate the capability of estimating and rejecting the disturbances, flight experiments are conducted under wind disturbances generated by a fan array wind tunnel (FAWT) from the Switzerland-based company WindShape. We first describe the hardware and software configurations of the UAV and the setup of the experiment. Afterwards, we present our experimental results including the characteristics of the wind disturbances and the control performance of the UAV when exposed to disturbances generated by the FAWT.

7.1. Hardware configuration

The multi-rotor UAV is shown in Figure 7. It has four brushless direct current electrical motors (T-Motor Air 2216 880-KV) paired with $10'' \times 4.5''$ carbon fiber propellers. To control the rotational speed of the motors, each is connected to an electronic speed control (T-Motor Air 20A), which receives commands from a PixHawk flight control unit (FCU, CUAU Nora plus) with redundant inertial measurement units (IMU). Flight control and state estimation are conducted by the FCU. The pose of the vehicle is measured by an optical motion capture system (VICON), and sent to a companion computer (Raspberry Pi 4) through Wi-Fi network, and then passed on to the FCU through a telemetry port. To generate wind fields with various turbulence characteristics for the flight experiments, we leveraged the Fan Array Wind Tunnel (FAWT) in Figure. 6. The wind tunnel is a 1.44 m by 0.72 m array of 162 independently controllable fans capable of generating wind speeds up to 12m/s. The distributed fans are controlled in real time by a Python program. In

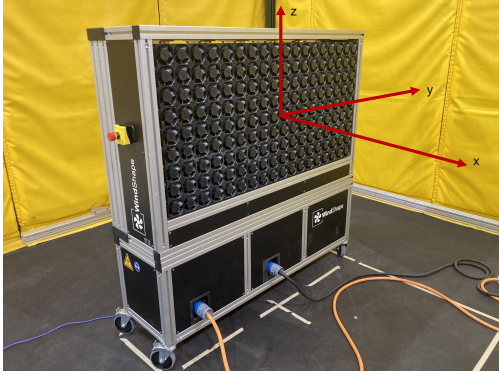


Figure 6: The FAWT and its body-fixed coordinate frame.



Figure 7: Quadrotor UAV developed in the autonomous unmanned system lab (AUSL) at Syracuse University.

our flight experiments, the FAWT was run at the steady uniform flow mode, with each individual fan running at identical and constant duty.

7.2. Software configuration

The flight control software is developed from the open-source autopilot software PX4 v1.13.2. According to Meier et al. (2015), the system architecture of PX4 is centered around a publish-subscribe object request broker on top of a POSIX application programming interface. This programming interface has different modules for data logging, communication, estimation, and control. The FFTS-ESO is implemented onto the module `mc_pos_control` and `mc_rate_control` for translational and rotational motions, respectively. The feedback of disturbance estimates from the FFTS-ESO is applied to the control law as an additional term, so that the original control architecture is modified with this feedforward disturbance rejection term. We introduce Boolean parameters to switch the disturbance rejection conveniently.

In the experiment, the rest of the autopilot (PX4 v1.13.2) is kept unchanged, to have a fair comparison of the flight control performance between the original PX4 autopilot, and the one with disturbance rejection from FFTS-ESO. The flight control parameters of the autopilot are as described in the multi-rotor frame S500 in <https://github.com/PX4/PX4-Autopilot/>. A Robot Operating System (ROS) interface program is developed for the companion computer that transmits commands and pose to the vehicle. The flight data are saved in the memory card inside the FCU in the form of .ulg file for post-processing. We use the MAVLINK telecommunication protocol for communication between the FCU, companion computer, and ground control station.

The FFTS-ESO parameters are selected as: $p = 1.2, k_{t1} = 6, k_{t2} = 3, k_{t3} = 1, \kappa_t = 0.6, k_{a1} = 8, k_{a2} = 4, k_{a3} = 2, \kappa_a = 0.6$. The empirically known mass and inertia of the vehicle as given to the FFTS-ESO are: $m = 1$ kg and $J = \text{diag}([0.03, 0.03, 0.06])$ kg · m². We link the source code of the customized PX4 with FFTS-ESO on Github.¹

7.3. Experiment procedure

The flight experiment setup is shown in Figure 8. We define the FAWT coordinate frame as shown in Figure 6, with x as the stream-wise direction, y as the span-wise direction, and z as

¹Github link: <https://github.com/nswang1994/GeometricPX4/tree/Geometric-FFTS-ESO>

the vertically up direction. The origin is at the geometric center of the fan array. We operate the FAWT at a steady uniform flow mode at 30%-70% of its maximum duty to measure the wind velocity of the wind field. We conduct the wind velocity measurements with a hotwire anemometer facing in the x direction at $x = 1.2\text{m}$, $y = 0\text{m}$, $z = 0\text{m}$ in the FAWT coordinate system.

As shown in Figure 8, the vehicle is commanded to hover in the front of the FAWT, at $x = 1.5\text{m}$, $y = 0\text{m}$, $z = 0\text{m}$ in the FAWT frame. This hovering position is at the center point of the test section, so that we can maximally avoid the boundary layer around the section border, where higher turbulence intensity and flow uncertainty occur. The time for hovering flight is set to 210 s. During this period, we turn on the FAWT for 150 s to disturb the vehicle with turbulent flows with statistically constant characteristics. The pose of the vehicle during flight is recorded in the log file for evaluation.

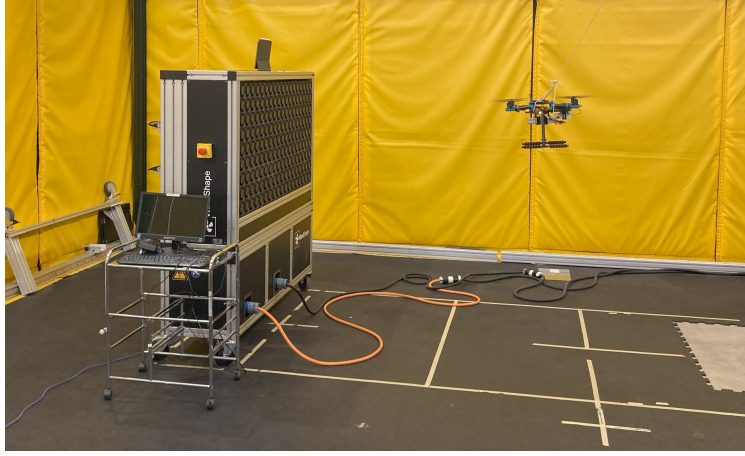


Figure 8: Setup for our flight control experiments.

7.4. Results: turbulent flow measurement

The results for hot-wire measurements are covered in this subsection. For brevity, we omit the details of the measurement procedure, which are accessible in the dissertation by Wang (2023). According to the Reynolds decomposition given in Pope (2000), we decompose the measured wind velocity u into the sum of a time-averaged velocity \bar{u} and fluctuating velocity \tilde{u} , such that $u = \bar{u} + \tilde{u}$, where (\cdot) stands for the time-averaged quantity. Based on hotwire measurements, we characterize the FAWT wind field with the following quantities: the time-averaged velocity \bar{u} , the variance of the fluctuating velocity $\overline{\tilde{u}^2}$, and the turbulence intensity (TI), which is defined by $\sqrt{\overline{\tilde{u}^2}}/\bar{u}$. We itemize the results as follows:

- $\bar{u}_{30} = 5.472 \text{ m/s}$; $\overline{\tilde{u}_{30}^2} = 0.061 \text{ m}^2/\text{s}^2$; $\text{TI}_{30} = 0.0451$;
- $\bar{u}_{40} = 6.876 \text{ m/s}$; $\overline{\tilde{u}_{40}^2} = 0.082 \text{ m}^2/\text{s}^2$; $\text{TI}_{40} = 0.0417$;
- $\bar{u}_{50} = 8.213 \text{ m/s}$; $\overline{\tilde{u}_{50}^2} = 0.116 \text{ m}^2/\text{s}^2$; $\text{TI}_{50} = 0.0415$;
- $\bar{u}_{60} = 9.590 \text{ m/s}$; $\overline{\tilde{u}_{60}^2} = 0.168 \text{ m}^2/\text{s}^2$; $\text{TI}_{60} = 0.0427$;
- $\bar{u}_{70} = 10.920 \text{ m/s}$; $\overline{\tilde{u}_{70}^2} = 0.237 \text{ m}^2/\text{s}^2$; $\text{TI}_{70} = 0.0446$.

To summarize, for the FAWT in the setup described earlier in this subsection, we observe that \bar{u} ranges from 5.472 m/s to 10.920 m/s, and TI is around 0.043. Moreover, we observe that $\overline{\tilde{u}^2}$ has positive correlation with \bar{u} . We assume that higher $\overline{\tilde{u}^2}$ brings higher turbulence energy, which causes higher disturbance inputs to the aircraft flying within the wind field.

7.5. Results: flight experiment

The results of the flight experiment are covered in this subsection. Figure 9 and Figure 10 illustrate the position and attitude tracking errors during hovering. The position tracking error is quantified as the Euclidean norm, while the attitude tracking error is quantified as the principal angle. To highlight the flight control performance under disturbances, we omit the pose data during take-off and landing in the presented result. The curves for the control scheme without disturbance rejection are plotted in blue, and those with disturbance rejection are in red. The time-averaged position and attitude tracking errors are listed in Table 3 .

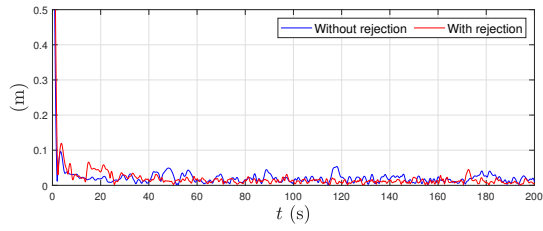
	Position tracking error (m)		Attitude tracking error (rad)	
	PX4 Stack	PX4+FFTS-ESO	PX4 Stack	PX4+FFTS-ESO
30%	0.0251	0.0236	0.0125	0.0116
40%	0.0468	0.0211	0.0140	0.0141
50%	0.0589	0.0254	0.0166	0.0132
60%	0.0792	0.0400	0.0164	0.0134
70%	Failed!	0.0557	Failed!	0.0139

Table 3: Time-averaged tracking error

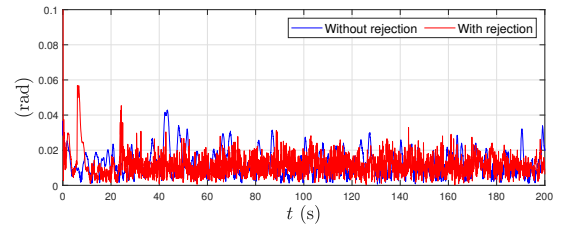
Figures 9 and 10 show that both position and attitude tracking errors have high transient at around 20s and 180s when the disturbances from FAWT kick in and fade off, respectively. In Figure 10, for the attitude tracking error of the control scheme with disturbance rejection, we observe extra transient at around 0s-10s, when the disturbance rejection kick-in. In Figure 9, we observe that when the FAWT operates at 40%-60% of its maximum duty, the position tracking error of the control scheme with disturbance rejection outperforms the one without rejection. When the FAWT operates at 30% of its maximum duty, the difference between the two control schemes is not evident in Figure 9. However, in terms of the time-averaged position tracking errors in Table 3, we can still observe that the scheme with disturbance rejection outperforms the one without rejection when the FAWT operates at 30%-60% of its maximum duty. When the FAWT operates at 70% of its maximum duty, the control scheme without disturbance rejection mechanism fails to hover constantly, while the one with rejection succeeds.

8. Conclusion

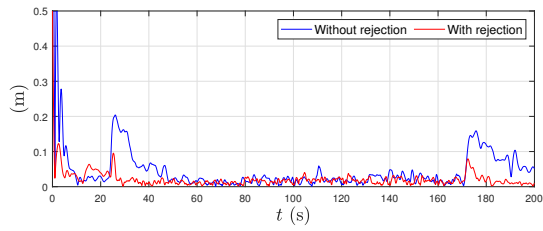
In this article, FFTS-ESO for disturbance estimation is designed for rotorcraft UAVs with a body-fixed thrust direction and three-axis attitude control. The vehicle is modeled as an under-actuated system on the tangent bundle of the six-dimensional Lie group of rigid body motions, SE(3). The proposed ESO scheme is developed based on the HC-FFTSD, which is similar to the STA used in sliding mode designs, to obtain fast finite-time stability with higher tunability of the



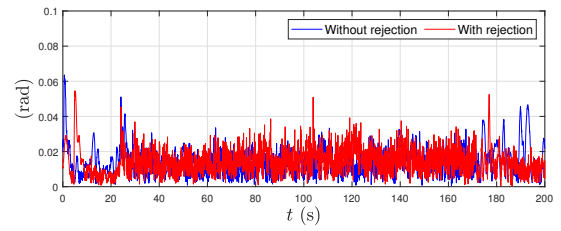
(a) Duty 30%



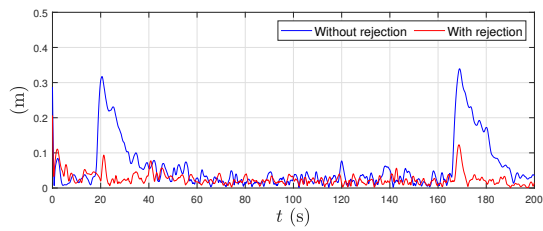
(a) Duty 30%



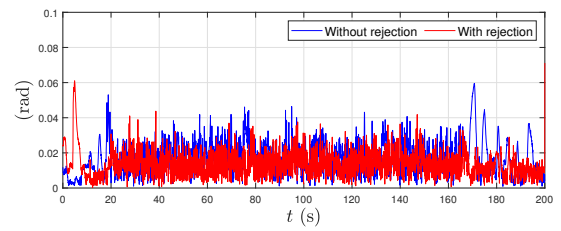
(b) Duty 40%



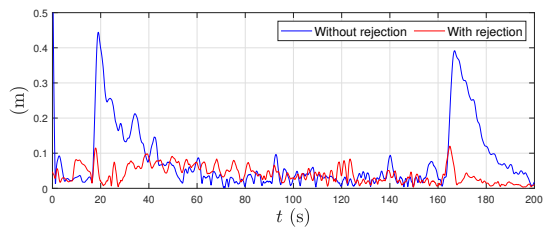
(b) Duty 40%



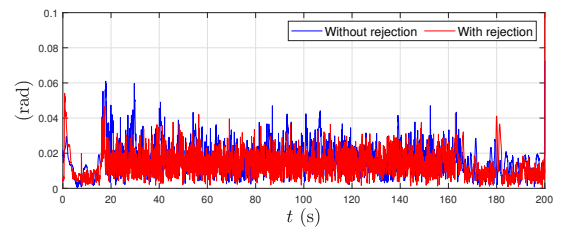
(c) Duty 50%



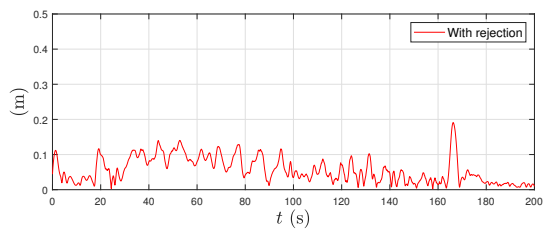
(c) Duty 50%



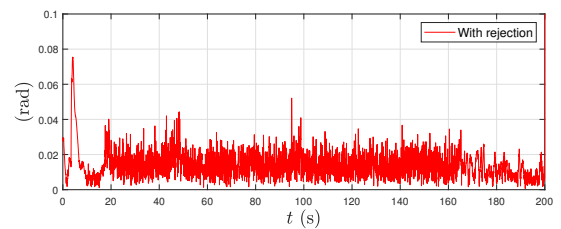
(d) Duty 60%



(d) Duty 60%



(e) Duty 70%



(e) Duty 70%

Figure 9: Position tracking error

Figure 10: Attitude tracking error

settling time compared to other FTS schemes. The Lyapunov stability analysis presented in this article for the ESO scheme proves the finite-time stability and robustness of the ESO on SE(3). A set of numerical simulations are conducted. The numerical simulation results present the stable performance of the FFTS-ESO scheme in estimating external force and torque disturbances acting on the UAV in different scenarios. The behavior of the FFTS-ESO is compared with two state-of-the-art observers for disturbance estimation. Using a realistic set of data for several simulated flight scenarios of a rotorcraft UAV, numerical simulations show that the FFTS-ESO, unlike the LESO and FxTSDO, is always stable and its convergence is robust to measurement noise and pose singularities. The proposed FFTS-ESO is implemented on the FCU of a multi-rotor UAV, with disturbance rejection control using feedback of disturbance estimates from the FFTS-ESO. The results validate the proposed FFTS-ESO experimentally and show the supremacy of the disturbance rejection control scheme over the original control scheme.

Appendix A. Proof of Lemma 5

Proof. Represent x as a linear combination of μ and ν :

$$x = c_1\mu + c_2\nu, \quad (\text{A.1})$$

where ν is a vector perpendicular to μ , such that $\mu^T\nu = 0$. Next, define two non-zero scalars, c_1, c_2 . Using (A.1), express Y in Lemma 5 in coordinates (c_1, c_2) :

$$Y = \frac{c_1\mu + c_2\nu}{(c_1^2\|\mu\|^2 + c_2^2\|\nu\|^2)^\alpha} - \frac{(1 + c_1)\mu + c_2\nu}{[(1 + c_1)^2\|\mu\|^2 + c_2^2\|\nu\|^2]^\alpha}.$$

Thereafter, we obtain its partial derivatives with respect to these coordinates:

$$\begin{aligned} \frac{\partial Y}{\partial c_1} &= \frac{\mu}{(c_1^2\|\mu\|^2 + c_2^2\|\nu\|^2)^\alpha} - \frac{2\alpha c_1\|\mu\|^2(c_1\mu + c_2\nu)}{(c_1^2\|\mu\|^2 + c_2^2\|\nu\|^2)^{\alpha+1}} \\ &\quad - \frac{\mu}{[(1 + c_1)^2\|\mu\|^2 + c_2^2\|\nu\|^2]^\alpha} + \frac{2\alpha(1 + c_1)\|\mu\|^2[(1 + c_1)\mu + c_2\nu]}{[(1 + c_1)^2\|\mu\|^2 + c_2^2\|\nu\|^2]^{\alpha+1}}, \end{aligned} \quad (\text{A.2})$$

$$\begin{aligned} \frac{\partial Y}{\partial c_2} &= \frac{\nu}{(c_1^2\|\mu\|^2 + c_2^2\|\nu\|^2)^\alpha} - \frac{2\alpha c_2\|\nu\|^2(c_1\mu + c_2\nu)}{(c_1^2\|\mu\|^2 + c_2^2\|\nu\|^2)^{\alpha+1}} \\ &\quad - \frac{\nu}{[(1 + c_1)^2\|\mu\|^2 + c_2^2\|\nu\|^2]^\alpha} + \frac{2\alpha c_2\|\nu\|^2[(1 + c_1)\mu + c_2\nu]}{[(1 + c_1)^2\|\mu\|^2 + c_2^2\|\nu\|^2]^{\alpha+1}}. \end{aligned} \quad (\text{A.3})$$

Thereafter, we employ the fact that the local maxima of Y^TY satisfy:

$$\frac{\partial}{\partial c_1}(Y^TY) = \frac{\partial}{\partial c_2}(Y^TY) = 0,$$

we obtain the following equivalent conditions for the maxima:

$$\nu^T \frac{\partial Y}{\partial c_1} = \mu^T \frac{\partial Y}{\partial c_2} = 0, \quad (\text{A.4})$$

$$\mu^T \frac{\partial Y}{\partial c_1} = 0, \quad (\text{A.5})$$

$$\nu^T \frac{\partial Y}{\partial c_2} = 0. \quad (\text{A.6})$$

Substituting (A.2) and (A.3) into (A.4), we obtain:

$$\begin{aligned}
\nu^T \frac{\partial Y}{\partial c_1} &= \mu^T \frac{\partial Y}{\partial c_2} = 0, \\
\iff -\frac{2\alpha c_1 c_2 \|\mu\|^2 \|\nu\|^2}{(c_1^2 \|\mu\|^2 + c_2^2 \|\nu\|^2)^{\alpha+1}} + \frac{2\alpha(1+c_1)c_2 \|\mu\|^2 \|\nu\|^2}{[(1+c_1)^2 \|\mu\|^2 + c_2^2 \|\nu\|^2]^{\alpha+1}} &= 0, \\
\implies c_1 [(1+c_1)^2 \|\mu\|^2 + c_2^2 \|\nu\|^2]^{\alpha+1} &= (1+c_1) [c_1^2 \|\mu\|^2 + c_2^2 \|\nu\|^2]^{\alpha+1},
\end{aligned} \tag{A.7}$$

Substituting (A.2) and (A.3) into (A.5), we obtain:

$$\begin{aligned}
\mu^T \frac{\partial Y}{\partial c_1} &= 0, \\
\implies \frac{(1-2\alpha \|\mu\|^2 c_1^2) \|\mu\|^2}{(c_1^2 \|\mu\|^2 + c_2^2 \|\nu\|^2)^{\alpha+1}} - \frac{[1-2\alpha(1+c_1)^2 \|\mu\|^2] \|\mu\|^2}{[(1+c_1)^2 \|\mu\|^2 + c_2^2 \|\nu\|^2]^{\alpha+1}} &= 0, \\
\iff (1+c_1)^2 = c_1^2, \iff c_1 &= -\frac{1}{2}.
\end{aligned} \tag{A.8}$$

Substituting (A.2) and (A.3) into (A.6), we obtain:

$$\begin{aligned}
\nu^T \frac{\partial Y}{\partial c_2} &= 0, \\
\implies \frac{(1-2\alpha \|\nu\|^2 c_2^2) \|\nu\|^2}{(c_1^2 \|\mu\|^2 + c_2^2 \|\nu\|^2)^{\alpha+1}} - \frac{(1-2\alpha \|\nu\|^2 c_2^2) \|\nu\|^2}{[(1+c_1)^2 \|\mu\|^2 + c_2^2 \|\nu\|^2]^{\alpha+1}} &= 0, \\
\iff (1+c_1)^2 = c_1^2, \iff c_1 &= -\frac{1}{2}.
\end{aligned} \tag{A.9}$$

(A.7) does not give a real solution for $\alpha \in]0, 1/2[$. Thus, we conclude that the only solution to (A.4), (A.5), (A.6) is given by $c_1 = -1/2, c_2 = 0$. Thus, the only critical value of $Y^T Y$ is obtained when $x = -\mu/2$. Further, we conclude that the global maximum of $Y^T Y$ is at $x = -\mu/2$ because it is positive definite in Y . Therefore, we do not need an analysis of the Hessian matrix of $Y^T Y$ as a function of (c_1, c_2) . \square

Acknowledgement

The authors acknowledge support from the National Science Foundation award 2132799 and WindShape Corp.

References

- Bangura, M. and Mahony, R. (2017). Thrust control for multirotor aerial vehicles. *IEEE Transactions on Robotics*, 33(2):390–405.
- Bhale, P., Kumar, M., and Sanyal, A. K. (2022). Finite-time stable disturbance observer for unmanned aerial vehicles. pages 5010–5015. 2022 American Control Conference (ACC).
- Bhat, S. P. and Bernstein, D. S. (2000a). Finite-time stability of continuous autonomous systems. *SIAM Journal on Control and optimization*, 38(3):751–766.
- Bhat, S. P. and Bernstein, D. S. (2000b). A topological obstruction to continuous global stabilization of rotational motion and the unwinding phenomenon. *Systems & control letters*, 39(1):63–70.

- Bisheban, M. and Lee, T. (2020). Geometric adaptive control with neural networks for a quadrotor in wind fields. *IEEE Transactions on Control Systems Technology*, 29(4):1533–1548.
- Bohn, J. and Sanyal, A. K. (2016). Almost global finite-time stabilization of rigid body attitude dynamics using rotation matrices. *International Journal of Robust and Nonlinear Control*, 26(9):2008–2022.
- Chaturvedi, N. A., Sanyal, A. K., and McClamroch, N. H. (2011). Rigid-body attitude control. *IEEE control systems magazine*, 31(3):30–51.
- Chen, C.-T. (1984). *Linear system theory and design*. Saunders college publishing.
- Chen, W.-H. (2003). Nonlinear disturbance observer-enhanced dynamic inversion control of missiles. *Journal of Guidance, Control, and Dynamics*, 26(1):161–166.
- Craig, W., Yeo, D., and Paley, D. A. (2020). Geometric attitude and position control of a quadrotor in wind. *Journal of Guidance, Control, and Dynamics*, pages 1–14.
- Cui, L., Zhang, R., Yang, H., and Zuo, Z. (2021). Adaptive super-twisting trajectory tracking control for an unmanned aerial vehicle under gust winds. *Aerospace Science and Technology*, 115:106833.
- Faessler, M., Franchi, A., and Scaramuzza, D. (2017). Differential flatness of quadrotor dynamics subject to rotor drag for accurate tracking of high-speed trajectories. *IEEE Robotics and Automation Letters*, 3(2):620–626.
- Guo, B.-Z. and Zhao, Z.-l. (2011). On the convergence of an extended state observer for nonlinear systems with uncertainty. *Systems & Control Letters*, 60(6):420–430.
- Hamrah, R. and Sanyal, A. K. (2022). Finite-time stable tracking control for an underactuated system in se (3) in discrete time. *International Journal of Control*, 95(4):1106–1121.
- Hanover, D., Foehn, P., Sun, S., Kaufmann, E., and Scaramuzza, D. (2021). Performance, precision, and payloads: Adaptive nonlinear mpc for quadrotors. *IEEE Robotics and Automation Letters*, 7(2):690–697.
- Hardy, G. H., Littlewood, J. E., Pólya, G., Pólya, G., et al. (1952). *Inequalities*. Cambridge university press.
- Hartlieb, R. J. (1956). The cancellation of random disturbances in automatic control systems. *PhDT*.
- Huang, Y., Xu, K., Han, J., and Lam, J. (2001). Flight control design using extended state observer and non-smooth feedback. volume 1, pages 223–228. Proceedings of the 40th IEEE Conference on Decision and Control (Cat. No. 01CH37228).
- Jia, J., Guo, K., Yu, X., Zhao, W., and Guo, L. (2022). Accurate high-maneuvering trajectory tracking for quadrotors: A drag utilization method. *IEEE Robotics and Automation Letters*, 7(3):6966–6973.
- Khalil, H. K. (2002). Nonlinear systems third edition. *Patience Hall*, 115.
- Lee, T., Leok, M., and McClamroch, N. H. (2010). Geometric tracking control of a quadrotor uav on se (3). pages 5420–5425. 49th IEEE conference on decision and control (CDC).
- Liu, K., Wang, R., Zheng, S., Dong, S., and Sun, G. (2022). Fixed-time disturbance observer-based robust fault-tolerant tracking control for uncertain quadrotor uav subject to input delay. *Nonlinear Dynamics*, 107(3):2363–2390.
- Liu, L., Wang, D., and Peng, Z. (2019). State recovery and disturbance estimation of unmanned surface vehicles based on nonlinear extended state observers. *Ocean Engineering*, 171:625–632.
- Mechali, O., Xu, L., Huang, Y., Shi, M., and Xie, X. (2021). Observer-based fixed-time continuous nonsingular terminal sliding mode control of quadrotor aircraft under uncertainties and disturbances for robust trajectory tracking: Theory and experiment. *Control Engineering Practice*, 111:104806.
- Meier, L., Honegger, D., and Pollefeys, M. (2015). Px4: A node-based multithreaded open source robotics framework for deeply embedded platforms. In *2015 IEEE international conference on robotics and automation (ICRA)*, pages 6235–6240. IEEE.
- Moeini, A., Lynch, A. F., and Zhao, Q. (2021). Exponentially stable motion control for multirotor uavs with rotor drag and disturbance compensation. *Journal of Intelligent & Robotic Systems*, 103(1):1–17.
- Moreno, J. A. and Osorio, M. (2012). Strict lyapunov functions for the super-twisting algorithm. *IEEE transactions on automatic control*, 57(4):1035–1040.
- Pope, S. B. (2000). *Turbulent flows*. Cambridge university press.
- Pounds, P., Mahony, R., and Corke, P. (2010). Modelling and control of a large quadrotor robot. *Control Engineering Practice*, 18(7):691–699.
- Rosier, L. (1992). Homogeneous lyapunov function for homogeneous continuous vector field. *Systems & Control Letters*, 19(6):467–473.
- Sanyal, A. (2022). Discrete-time data-driven control with hölder-continuous real-time learning. *International Journal of Control*, 95(8):2175–2187.
- Sanyal, A., Nordkvist, N., and Chyba, M. (2010). An almost global tracking control scheme for maneuverable autonomous vehicles and its discretization. *IEEE Transactions on Automatic control*, 56(2):457–462.
- Sanyal, A. K. and Bohn, J. (2015). Finite-time stabilisation of simple mechanical systems using continuous feedback.

- International Journal of Control*, 88(4):783–791.
- Shao, X., Liu, J., Cao, H., Shen, C., and Wang, H. (2018). Robust dynamic surface trajectory tracking control for a quadrotor UAV via extended state observer. *International Journal of Robust and Nonlinear Control*, 28(7):2700–2719.
- Torrente, G., Kaufmann, E., Föhn, P., and Scaramuzza, D. (2021). Data-driven mpc for quadrotors. *IEEE Robotics and Automation Letters*, 6(2):3769–3776.
- Vidal, P. V., Nunes, E. V., and Hsu, L. (2016). Output-feedback multivariable global variable gain super-twisting algorithm. *IEEE Transactions on Automatic Control*, 62(6):2999–3005.
- Viswanathan, S. P., Sanyal, A. K., and Samiei, E. (2018). Integrated guidance and feedback control of underactuated robotics system in se (3). *Journal of Intelligent & Robotic Systems*, 89(1):251–263.
- Viswanathan, S. P., Sanyal, A. K., and Warier, R. R. (2017). Finite-time stable tracking control for a class of underactuated aerial vehicles in se (3). pages 3926–3931. 2017 American control conference (ACC).
- Wang, N. (2023). Geometric active disturbance rejection control for autonomous rotorcraft in complex atmospheric environment.
- Wang, N. and Sanyal, A. K. (2021). A hölder-continuous extended state observer for model-free position tracking control. In *2021 American Control Conference (ACC)*, pages 2133–2138. IEEE.
- Wang, N. and Sanyal, A. K. (2022). A hölder-continuous extended state observer for rigid body attitude dynamics. *IFAC-PapersOnLine*, 55(22):340–345.
- Xia, Y., Zhu, Z., Fu, M., and Wang, S. (2010). Attitude tracking of rigid spacecraft with bounded disturbances. *IEEE Transactions on Industrial Electronics*, 58(2):647–659.
- Yu, S., Yu, X., Shirinzadeh, B., and Man, Z. (2005). Continuous finite-time control for robotic manipulators with terminal sliding mode. *Automatica*, 41(11):1957–1964.
- Zhu, Z., Xia, Y., and Fu, M. (2011). Attitude stabilization of rigid spacecraft with finite-time convergence. *International Journal of Robust and Nonlinear Control*, 21(6):686–702.